Monthly Notices
of the
ROYAL ASTRONOMICAL SOCIETY

MNRAS **469,** 1655–1672 (2017)
Advance Access publication 2017 April 17

doi:10.1093/mnras/stx891

The prolonged X-ray flaring activity of Mrk 501 in 2014

B. Kapanadze,[1,2★] D. Dorner,[3] P. Romano,[2] S. Vercellone,[2] K. Mannheim,[3] E. Lindfors,[4] K. Nilsson,[5] R. Reinthal,[4] L. Takalo,[4] S. Kapanadze[1] and L. Tabagari[1]

[1] *E. Kharadze Abastumani Astrophysical Observatory, Ilia State University, Colokashvili Av. 3/5, Tbilisi 0162, Georgia*
[2] *INAF, Osservatorio Astronomico di Brera, Via E. Bianchi 46, I-23807 Merate, Italy*
[3] *Institute for Theoretical Physics and Astrophysics, Universität Würzburg, Emil-Fischer-Str. 31, D-97074 Würzburg, Germany*
[4] *Tuorla Observatory, Department of Physics and Astronomy, University of Turku, FI-20014 Turku, Finland*
[5] *Finnish Centre for Astronomy with ESO (FINCA), University of Turku, Väisäläntie 20, FI-21500 Piikkiö, Finland*

Accepted 2017 April 7. Received 2017 April 7; in original form 2017 February 2

ABSTRACT

The X-ray variability of the BL Lacertae source Mrk 501 was studied during 11.5 yr of monitoring with *Swift*. Here, we report the results of this study pertaining to the epoch of 2014 March–October, when our target showed the most powerful and long-lasting X-ray flaring activity. This epoch was characterized by X-ray flares varying in amplitude by factors of 2–5 on time-scales of a few weeks or shorter. We detected 35 instances of the intraday variability, sometimes occurring within the 1 ks observational runs. The X-ray flux was generally correlated with the TeV flux, while the 0.3–300 GeV and optical-UV fluxes did not show a significant correlation. Some notable incidences of more complicated variability patterns could also be recognized, indicating that the high-energy emission in Mrk 501 arose from an emission region more complex than a single zone. The best fits of the 0.3–10 keV spectra were mainly obtained using the logparabola model. Strong spectral variability was detected, affecting the slope but not the curvature of the spectrum. In strong flares, the spectral index became harder than 1.70. The spectral evolution was characterized by a harder-when-brighter behaviour, shifting the peak of the spectral energy distribution by about 20 keV that happens rarely in blazars.

Key words: BL Lacertae objects: individual: Mrk 501.

1 INTRODUCTION

BL Lacertae objects (BLLs) are widely accepted to be active galactic nuclei (AGNs) with a relativistic jet closely aligned to our line of sight (Blandford & Rees 1978 and references therein). This interpretation is successful in explaining their observational features like weak or absent emission lines, compact and flat-spectrum radio emission, superluminal motions, high radio and optical polarization, non-thermal continuum extending from the radio to the very high-energy (VHE) γ-rays, double-humped spectral energy distribution (SED; in the ν–νF_ν representation), significant flux variability in all spectral bands (Falomo, Pian & Treves 2014). The lower energy SED component is explained by synchrotron radiation emitted by relativistic electrons in the jet, while an inverse Compton (IC) scattering of synchrotron photons by the same electron population (SSC; Marscher & Gear 1985), ambient photons scattered by the jet electrons (EC; Dermer, Schlickeiser & Mastichiadis 1992), hadronic processes (Mannheim & Biermann 1992), etc. are considered as possible sources for the high-frequency bump.

In this paper, we report about a strong and prolonged X-ray flaring activity of the nearby ($z = 0.034$; Ulrich et al. 1975) high-energy peaked BLL source (HBL, i.e. a BLL with a synchrotron component peaking in at the UV-X-ray frequencies; Padovani & Giommi 1995) Mrk 501 revealed by the observations performed with the X-ray Telescope (XRT; Burrows et al. 2005) onboard the *Swift* satellite (Gehrels et al. 2004). This HBL is a bright X-ray source, and the second extragalactic source detected in the TeV band (Quinn et al. 1996) that made Mrk 501 a target of several multiwavelength (MWL) campaigns (Pian et al. 1998; Aharonian et al. 1999). Along with the XRT data, we have analysed those obtained with the Ultraviolet-Optical Telescope (UVOT; Roming et al. 2005) and the Burst Alert Telescope (BAT; Barthelmy et al. 2005) onboard *Swift*. We also constructed light curves for the same period using the publicly available VHE [First G-APD Cherenkov Telescope (FACT); Anderhub et al. 2009, high energy [HE, $E > 1$ MeV, Large Area Telescope (LAT) onboard *Fermi*; Atwood et al. 2009, optical (Steward and Tuorla observatories) and radio (the OVRO 40-m telescope; Richards et al. 2011) data to draw conclusions about

★ E-mail: bidzina_kapanadze@iliauni.edu.ge

the target's long-term MWL behaviour and to search for interband cross-correlations.

The paper is organized as follows. Section 2 describes the data processing and analysing procedures. In Section 3, we provide the results of a timing and spectral analysis. We discuss our results in Section 4, and provide our conclusions in Section 5.

2 OBSERVATIONS AND DATA REDUCTION

2.1 X-ray data

Level 1 unscreened XRT event files were processed with the XRTDAS package developed at the ASI Science Data Center (ASDC) and distributed by HEASARC within the HEASOFT package (v.6.19). They were reduced, calibrated and cleaned by means of the XRTPIPELINE script using the standard filtering criteria and the latest calibration files of *Swift* CALDB v.20160731. We selected the events with the 0–2 grades for the Windowed Timing (WT) mode, used to observe Mrk 501. The source and background light curves and spectra were extracted with XSELECT using the circular area with radii 20–50 pixels depending on the source brightness and exposure. The light curves were then corrected using the XRTLCCORR task for the resultant loss of effective area, bad/hot pixels, pile-up and vignetting. The ancillary response files (ARFs) were generated using the XRTMKARF task, with the corrections applied to account for the PSF losses, different extraction regions, vignetting and CCD defects. The latest response matrix from the XRT calibration files has been used. The instrumental channels were combined to include at least 20 photons per bin using the GRPPHA task. After selecting the best-fitting model for the fixed hydrogen absorption column density $N_{\rm H}$ and deriving the values of corresponding spectral parameters (see Section 3.2 for details), we calculated the unabsorbed 0.3–2, 2–10 and 0.3–10 keV fluxes using the cflux model.

From the publicly available weekly binned light curves of Mrk 501 obtained with *MAXI*,[1] we used only those data corresponding to the source's detection above the 5σ significance for a flux variability study.[2] The BAT data, taken from the *Swift*-BAT Hard X-ray Transient Monitor programme[3] (Krim et al. 2013), have been re-binned using the tool REBINGAUSSLC from the HEASOFT package using the weekly bins.

2.2 UV, optical and radio data

The sky-corrected UVOT images in the bands *V*, *B*, *U*, *UVW1*, *UVM2* and *UVW2* were processed using the standard UVOT software developed and distributed within HEASOFT and the calibration files included in the CALDB. The UVOTSOURCE tool was used to extract the source and background counts, correct for coincidence losses, apply background subtraction, and calculate the corresponding magnitude and error. The measurements were performed using the 5 arcsec radius source aperture for *V, B, U* bands and the 10 arcsec radius for *UVW1*, *UVM2*, *UVW2* bands, since the source was significantly brighter at UV frequencies. The magnitudes were then corrected for the Galactic absorption applying $E(B-V) = 0.023$ mag (using the recipe of Güver & Özel 2009) and the $A_\lambda/E(B-V)$ values, derived from interstellar extinction curves provided in Fitzpatrick & Massa (2007). The effective wavelength of each UVOT filters were taken from Poole et al. (2008). We converted them into linear fluxes (in mJys) adopting the latest photometric zero-points for each band provided in Breeveld et al. (2011).

During 2014 March–October, Mrk 501 was monitored intensively in the *R* band of the Cousins system with the 35-cm telescope attached to the 60-cm Kungliga Vetenskapsakademi (KVA) telescope (La Palma, Spain). The data are analysed using the semi-automatic pipeline developed at Tuorla Observatory (Lindfors et al. 2016). The magnitudes are derived using the differential photometry and comparison stars from Villata et al. (1998). The magnitudes are dereddened using the $A_{\rm R}$ value from NED and converted into Janskys via the standard formula $F = 3080 \times 10^{0.4 \times {\rm mag}}$. The host contribution is subtracted from the total flux according to Nilsson et al. (2007).

We extracted the publicly available *V*- and *R*-band data obtained with the 2.3-m Bock and 1.54-m Kuiper telescopes of Steward observatory[4] during 2009–2016 (see Smith et al. 2009 for details). We have de-reddened and converted the corresponding magnitudes into linear fluxes similar to the KVA data, although the obtained values are not corrected for the host contribution since the host's *V*- and *R*-band values of Mrk 501 from the Steward observations are not available.

Regular 15 GHz observations of Mrk 501 were carried out as part of the blazar monitoring programme at Owens Valley Radio Observatory (OVRO) using the 40 m telescope that includes all the *Fermi*-detected blazars with $\delta > -20^\circ$ (Richards et al. 2011). We retrieved the publicly available OVRO data of our target from the corresponding website.[5] The details of the data reduction and calibration procedure can be found in Richards et al. (2011).

2.3 γ-ray data

We extracted the 300 MeV–300 GeV fluxes from the LAT observations using the events of diffuse class from a region of interest (ROI) of radius 10°, centred on Mrk 501, and processed with the *Fermi* SCIENCETOOLS package (v.10r0p5) with P8R2_V6 instrument response function. A cut on the zenith angle ($>100^\circ$) was applied to reduce contamination from the Earth-albedo γ-rays. Data with a rocking angle of the spacecraft larger than 52° are discarded to avoid contamination from photons from the Earth's limb. A background model including all γ-ray sources from the *Fermi*-LAT 4-yr Point Source Catalog (3FGL; Acero et al. 2015) within 20° of Mrk 501 was created. The remaining excesses in the ROI were modelled as point sources with a simple power-law spectrum. The spectral parameters of sources within the ROI are left free during the minimization process, while those outside of this range were held fixed to the 3FGL catalogue values. The Galactic and extragalactic diffuse γ-ray emission as well as the residual instrumental background are included using the recommended model files GLL_IEM_V06.FITS and ISO_P8R2_SOURCE_V6_V06.TXT. The photon flux, spectral parameters and test-statistics (TS) for the source are computed using an unbinned likelihood analysis method GTLIKE. For the spectral modelling of Mrk 501, we adopted a simple power law, as done in the 3FGL catalogue. In a few cases, the source was not detectable with 3σ significance from the 3-d bins, and we calculated the upper limit to the photon flux using the CALCUPPER tool.

Mrk 501 is one of the sources regularly monitored by the FACT at TeV energies. This imaging air Cherenkov telescope is located in the

[1] http://maxi.riken.jp/
[2] Mihara, private communication.
[3] http://swift.gsfc.nasa.gov/results/transients/
[4] See http://james.as.arizona.edu/psmith/Fermi/
[5] See http://www.astro.caltech.edu/ovroblazars/

Table 1. Extract from the summary of the XRT observations of Mrk 501 in 2014 March–October. The columns are as follows: (1) – observation ID; (2) – observation start and end, respectively (in UTC); (3) – exposure (in seconds); (4)–(7): mean value of the observed flux with its error (in cts s^{-1}), reduced χ^2 with corresponding d.o.f., bin size, existence of a variability during the observation (V stands for a variability detection; PV – possibly variable; NV – non-variable), respectively.

ObsID (1)	Obs. Start–End (UTC) (2)	Exposure (s) (3)	CR (cts s^{-1}) (4)	χ^2/d.o.f. (5)	Bin (s) (6)	Var. (7)
00091745028	03-01 20:45:59 21:51:56	1004	9.12 (0.1)	0.368/7	120	NV
00091745029	03-03 22:12:59 23:20:08	1024	9.11 (0.10)	1.543/7	120	NV
00091745030	03-05 09:33:58 10:40:33	970	8.68 (0.10)	1.028/7	120	NV

Observatorio del Roque de los Muchachos (La Palma, Spain) and operational since 2011 October. Since 2012 December, the FACT collaboration publishes the results of a preliminary quick-look analysis with low latency on a website.[6] These background-subtracted light curves are not corrected for the effect of changing energy threshold with changing zenith distance and ambient light, and no data selection is done. The details of the quick-look analysis are described in Dorner et al. (2015). In total, almost 1500 h of data are available for Mrk 501 from the FACT quick-look analysis between 2012 December and 2016 May. For our study, we have restricted the sample to nights with a signal detected with a minimum significance of 3σ. From the daily-binned data, we used 84 nights (205 h) for the study in 2014 and 190 nights (484 h) in total. More than 96 per cent of these data are taken with a zenith distance small enough to not influence significantly the energy threshold of the analysis. More than 86 per cent of the data are taken under light conditions not increasing the analysis threshold significantly. The nightly observation time was between 0.3 and 5.2 h.

3 RESULTS

3.1 Flux variability

3.1.1 Long-term X-ray variability

The source was observed by the XRT 100 times between 2014 March 1 and October 16, including our target of opportunity observations during May 24–26. The information about each pointing and the measurement results are provided in Table 1.[7] The UVOT results are presented in Table 2, where the de-reddened magnitudes and corresponding fluxes are provided for each band.

The historical light curve of Mrk 501 from XRT observations (Fig. 1a) shows that the source exhibited the most extreme X-ray flare during the 11.5-yr period in 2014 March–October when the 0.3–10 keV count rate varied by a factor of 4.7 up to 21.52 ± 0.16 cts s^{-1} (Fig. 2a), and the weighted mean count rate $\overline{CR}_{2014} = 11.14 \pm 0.01$ cts s^{-1} is a factor of 2.1 larger than that from the rest XT observations. Although the source showed a prolonged X-ray flaring activity also in 2012 (during MJD 55840–56140) and the source reached its highest historical 0.3–10 keV brightness that for that time, the period presented here was prominent with significantly higher fluxes and more extreme spectral properties.

Fig. 2a shows that the source underwent several shorter term X-ray flares on time-scales of a few weeks in 2014 March–October (see Section 3.1.3 for their detailed description). In this period, the source was detected 15 times with 5σ significance from the weekly binned BAT observations that showed a variability by a factor of 3.1, and the peak of the BAT light curve coincides with the epoch of one of the short-term X-ray flares (Fig. 2d). Note that the historical BAT light curve of Mrk 501 is the most densely sampled in 2014 March–October (see Fig. 1d). Mrk 501 was detected 14 times in the 2–20 keV band by *MAXI* with 5σ significance, and the maximum-to-minimum flux ratio $R = 2.75$ (Fig. 2e). Due to the sparsely sampled light curve, the flares are not clearly recorded, although the historical 2–20 keV light curve shows that the source showed the highest rate in this period (see Fig. 1e).

3.1.2 Long-term variability in other spectral bands

In this period, the source was detected above the 3σ significance 85 times in 2015 March–October from the daily-binned FACT data that amounts to 50 per cent of all detections of Mrk 501 during 2013–2016 (since the start of the FACT observations of our target). The source exhibited a strong TeV-variability with maximum-to-minimum flux ratio $R = 20.6$ (see Fig. 2b), and this large value is mainly due to the very fast and strong outburst by a factor of 5 on MJD 56731–56732 (June 23–24) on the energies above 750 GeV. Note that this event was detected also with The High Energy Stereoscopic System (HESS) that revealed a flare by a factor of 5.5 with a flux doubling time of a few minutes for the energies greater than 2 TeV (Chakraborty et al. 2015). Note that the source underwent a very strong TeV flare by a factor of 7.4 in 2013 February (MJD 56332–56344; see Fig. 1b), but its peak flux value was by 22 per cent lower than that in 2014 June. The source was mostly detectable from the 3-d binned LAT data, and the 0.3–300 GeV flux exhibited a variability on time-scales of a few weeks (Fig. 2c). Among several short-term flares, the strongest one by a factor of 3.95 was recorded during MJD 56906–56922 when *Swift* did not observe our target. Fig. 1c exhibits that Mrk 501 was not as strongly variable in the LAT band as in X-rays during 2014 March–October (see Section 4.2 for the discussion).

The source showed a much weaker and slower variability with maximum-to-minimum flux ratio $R = 1.48$–2.00 in the *UVW1*, *UVM2* and *UVW2* bands compared to the X-ray-TeV energy range (Fig. 2f). In many cases, the source did not undergo an increasing UV activity and sometimes it showed a decreasing trend or a minimum along with strong X-ray flares. The highest historical UV state was observed in 2012 October, in contrast to the higher energy bands, and 2014 March–October was not the period of highest historical UV fluxes (see Fig. 1f). A similar behaviour is evident also in the optical UVOT bands (Fig. 2g), where the variability was even smaller with maximum-to-minimum flux ratio $R = 1.07$–1.26 that should be partially related to the significant contribution from the bright host galaxy and much sparsely sampled observations compared to the *UVW1*–*UVW2* bands. The *V*- and *R*-band light curves,

[6] http://www.fact-project.org/monitoring

[7] The printed version of the paper presents the extracts from Tables 1, 2, 4, 5, 8 and Fig. 10. Their full versions are available online. Fig. 9 is completely included in the online material.

Table 2. Extract from the results of the UVOT observations. The flux values in each band are given in units of mJy.

	V		*B*		*U*		*UVW1*		*UVM2*		*UVW2*	
ObsID	Mag.	Flux	Mag.	Flux	Mag.	Flux	Mag.	Flux	Mag.	Flux	Mag.	Flux
91745028	13.21 (0.02)	19.05 (0.32)	13.88 (0.03)	11.38 (0.33)	13.64 (0.02)	5.06 (0.11)	13.76 (0.03)	2.81 (0.10)	13.67 (0.02)	2.61 (0.06)	13.66 (0.03)	2.54 (0.07)
91745029	13.15 (0.02)	20.14 (0.32)	13.89 (0.03)	11.27 (0.33)	13.60 (0.03)	5.25 (0.11)	13.67 (0.03)	3.05 (0.10)	13.59 (0.03)	2.81 (0.06)	13.63 (0.03)	2.61 (0.07)
91745030	13.18 (0.02)	19.59 (0.32)	13.89 (0.03)	11.27 (0.33)	13.58 (0.03)	5.35 (0.11)	13.71 (0.03)	2.94 (0.10)	13.67 (0.03)	2.61 (0.06)	13.71 (0.03)	2.42 (0.06)

constructed via the data obtained at the Steward observatory, both yield a maximum-to-minimum flux ratio of 1.28 (including the host contribution; see Fig. 1h). In this period, the source was observed significantly frequently with the KVA telescope in the *R* band, and the corresponding light curve does not show a large variability (with maximum-to-minimum flux ratio of 1.36; Fig. 2h).

Finally, a very weak and slow variability by about 10 per cent is evident from the 15 GHz light curve (see Fig. 2i), constructed on the basis of the OVRO observations performed in 2014 March–October. The historical light curve shows that the source was in intermediate radio states in the period presented here, and significantly brighter states were observed in 2010 (Fig. 1i), similar to the optical-UV bands.

Below, we concentrate on the results from the different periods (based on the occurrence of shorter term flares on time-scales of a few weeks in the XRT band) from 2014 March to 2014 October whose summary is presented in Table 3. For each flare, the fractional root mean square (rms) variability amplitude and its error were calculated according to Vaughan et al. (2003). The MWL light curves from each period are provided in Fig. 3.

3.1.3 Shorter term flares

The source underwent a slow decline in the X-ray brightness during Period 1 (see Table 3) that lasted about 2 weeks (Fig. 3a). The LAT flux showed a peak after 4.5 d since the start of this period, and then it dropped by a factor of 2.4 in 3 d. The UV and optical fluxes also showed an uncorrelated variability with respect to the X-ray flux. In Period 2, the 0.3–10 keV flux showed an increase by 50 per cent in 4 d, then showed minor fluctuations around the level of 9.5 cts s^{-1} during $\sim$1 month, before reaching its peak in this period (Fig. 3b). Note that the LAT and UVOT-band fluxes showed two consequent flares (although the optical-UV variability was weaker than the HE one), and their second peak coincided with that of the XRT light curve. The 0.3–300 GeV light curve nearly followed the XRT one during MJD 56730–56744, but then showed a drop by a factor of 4.8, in contrast to the latter.

Period 3 (see Table 3) was characterized by the strongest short-term X-ray flare by a factor of 4.6 in 22 d, followed by a very fast decay by a factor of 2.6 in 2 d (Fig. 3c). Meanwhile, the LAT-band and optical-UV fluxes showed only very few variability and a lack of the correlation with the X-ray one. The source showed a brightening by 57 per cent during the initial 2-weeks part of Period 4, followed by smaller-amplitude fluctuations around the level of 14 cts s^{-1} during the next 3 weeks (see Fig. 3d). This period was also characterized by relatively densely sampled FACT light curve (30 detections above the 3σ significance) and by a very strong and fast TeV outburst centred on MJD 56831 that was accompanied by 19 per cent increase in the 0.3–10 keV flux. The 0.3–300 GeV and optical-UV light curves did not exhibit any correlation with that from the XRT band.

The source attained its largest historical 0.3–10 keV brightness state in Period 5 when it underwent a flare by a factor 2.1, and we observe another, relatively low peak after 9 d (see Fig. 3e). The FACT light curve shows a correlated behaviour with that of the XRT band but the second TeV peak is significantly higher than the first one. Similar to previous period, the UV fluxes did not show any correlation with the 0.3–10 keV one, and the LAT-band light curve shows an enhanced γ-ray activity only in the epoch of the second X-ray peak.

In Period 6, the 0.3–10 keV light curve is similar to that from the previous period. However, its peaks are lower and separated

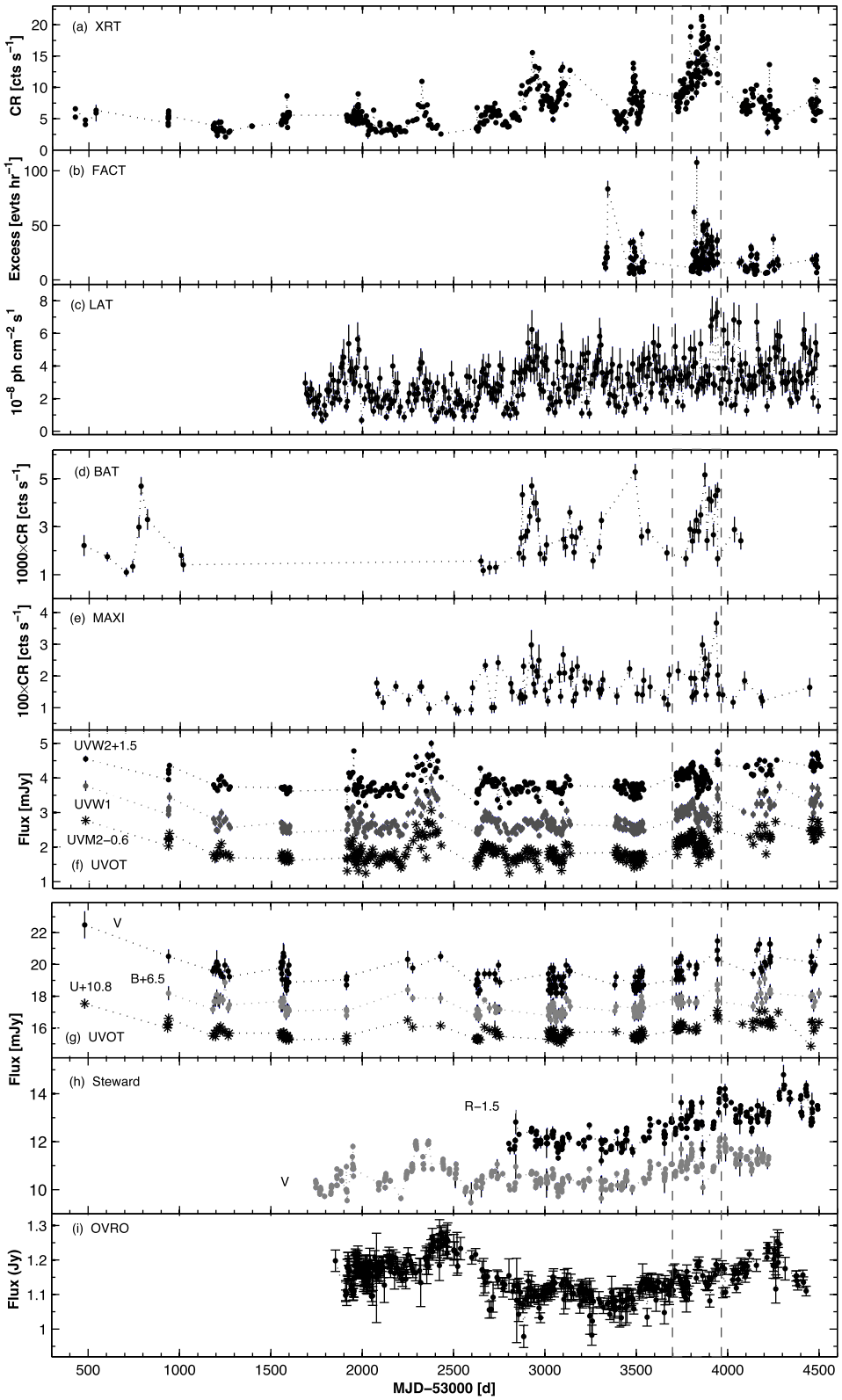

Figure 1. The historical light curves of Mrk 501 from the MWL observations performed in 2005–2016 with XRT (top panel), FACT (panel b), LAT (panel c), BAT (panel d), MAXI (panel e), UVOT (panels f–g), Steward Observatory (panel h) and OVRO (panel i). We used daily bins for XRT, FACT, UVOT, Steward, OVRO data and one-week bins for those of *MAXI*, LAT, BAT observations. The light curves between the vertical dashed lines belong to the period 2014 March–October.

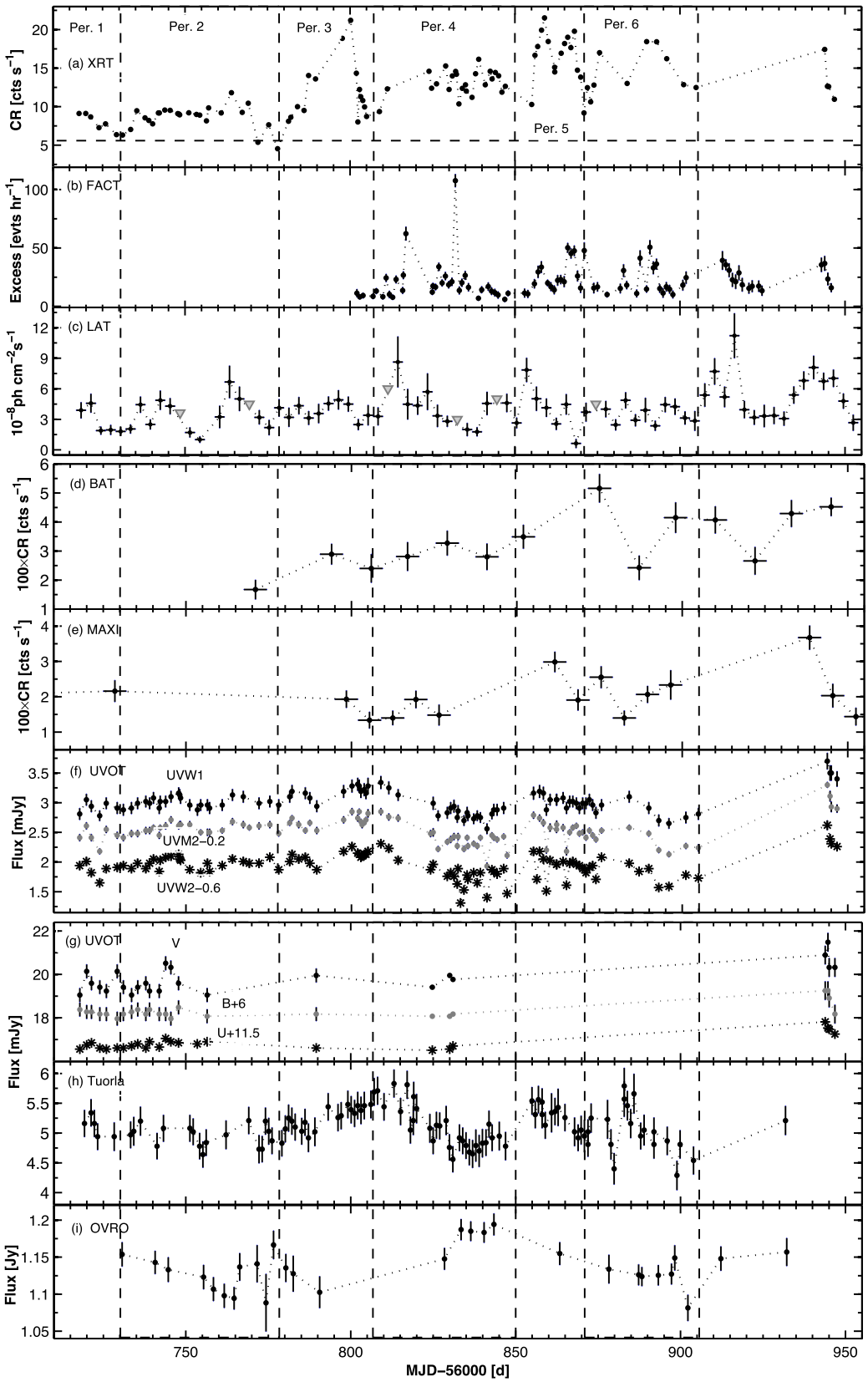

Figure 2. Same as Fig. 1 for the period 2014 March–October (with an exclusion for panel h, where we used densely sampled Tuorla data for a light-curve construction). We used daily bins for XRT, FACT, UVOT, Steward, OVRO data, 3-d bins for the LAT observations and 1-week bins for those performed with BAT and *MAXI*. The vertical dashed lines indicate the periods discussed in Section 3.1. The horizontal dashed line in the top panel stands for the weighted mean count rate from the XRT observations of Mrk 501 in 2005–2016 (excluding the 2014 March–October observations). Grey triangles in Panel d denote upper limits to the LAT flux when the source was detected below the 3σ significance.

Table 3. Summary of the XRT, UVOT, OVRO, Tuorla, *MAXI*, LAT and FACT observations in different periods. Columns 3–5: maximum 0.3–10 keV flux in cts s^{-1}, maximum-to-minimum flux ratio and fractional amplitude (per cent) for each flare, respectively; Columns 6–7: maximum-to-minimum flux ratios for unabsorbed 0.3–2 and 2–10 keV fluxes; Columns 8–10: the same for the UVOT bands *UVW1, UVW2, UVW2*, and those for *MAXI*, OVRO, LAT and FACT in Columns 11–13. For the calculation of the quantity R in each band, we used the thresholds referred in Section 2.

		XRT					UVOT			OVRO	Tuor.	*MAXI*	LAT	FACT
Per.	Dates	F_{max}	R	F_{var}	R_{2-10}	$R_{0.3-2}$	R_{UVW2}	R_{UVM2}	R_{UVW1}	R	R	R	R	R
(1)	(2)	(3)	(4)	(5)	(6)	(7)	(8)	(9)	(10)	(11)	(12)	(13)	(14)	(15)
1	March 1–13	9.12 (0.10)	1.44	15.4 (0.5)	1.76	1.47	1.16	1.18	1.10	–	1.08	1.85	2.53	–
2	March 15–May 1	11.81 (0.12)	2.60	17.8 (0.3)	3.14	2.47	1.13	1.11	1.10	1.07	1.12	2.13	6.40	–
3	May 1–28	21.20 (0.16)	4.66	36.5 (0.6)	8.13	3.80	1.16	1.14	1.13	1.03	1.18	1.95	1.98	1.39
4	May 31–July 9	16.15 (0.13)	1.85	12.0 (0.2)	2.54	1.80	1.52	1.42	1.30	1.04	1.28	5.05	4.85	13.9
5	July 17–August 1	21.52 (0.16)	2.34	20.5 (0.2)	3.82	3.15	1.32	1.26	1.11	–	1.13	1.69	4.18	3.57
6	August 4–September 4	18.43 (0.14)	1.74	21.2 (0.6)	2.47	1.56	1.24	1.19	1.17	1.06	1.35	3.09	2.05	4.99

by larger time interval from each other (∼2 weeks; Fig. 3f) than in the case of Period 5. The FACT data revealed a fast flare that preceded by about 2 d an X-ray brightening by 60 per cent during MJD 56873–56875 and showed low TeV states around the first X-ray peak observed in this period. However, it showed two fast flares by a factor of 3.4–3.7 in the second part of this period, when the source exhibited an enhanced activity also in the XRT band. Once again, the LAT and UVOT-band fluxes did not show any correlation with the X-ray one.

3.1.4 Intraday variability

We performed a search for intraday X-ray flux variability (IDV, i.e. a flux change within a day; Wagner & Witzel 1995) by means of the χ^2-statistics. Generally, we used 60-s bins for a light-curve construction in this study. For some observations, however, we also used the 120-s or orbit-binned data when the value of χ^2 was close to the threshold necessary for the detection of an IDV in the case of 60-s binning. We detected 35 instances of the 0.3–10 keV IDVs at the 99.9 per cent confidence level. For each event, the values of reduced χ^2 and fractional variability amplitude are provided in Table 4. The ranges of the spectral parameters a, b and E_p (see Section 3.2 for their definitions) are also given along with each event, derived with the logparabolic of power-law spectral models (see below).

The fastest variability was recorded on May 4 when the source brightened by 26 per cent in 240 s and then declined by 37 per cent in 420 s during the second part of the observation (Fig. 4a). The source was active on intraday time-scales during May 23–28 when the brightness initially decreased by 45–78 per cent a day, then the flux increased by 52 per cent within 1 d (Fig. 4b). We observe a decline by 38 per cent during the first 450-s segment of the May 31 pointing (Fig. 4c) and fast brightness fluctuations by ∼10 per cent within 400 s on June 30. As for other IDVs, they occurred during the observations consisting of two orbits separated by 1–23.5 h from each other, and their details are provided in Table 4.

We have found the seven IDVs at the 99.5 per cent confidence level (so-called possible variability; Andruchow, Romero & Cellone 2005) whose summary is also given in Table 4. Figs 4(e)–(h) present the most extreme four cases with brightness fluctuations by 13–26 per cent within 360–720 s and fractional amplitudes F_{var} = 3.4–6.7 per cent.

Our timing study of long-term XRT monitoring of Mrk 501 during 2014 March–October has revealed that the source was highly variable on weeks-to-month time-scales by a factor of 1.5–4.7, and it showed X-ray IDVs characterized by fractional variability amplitudes of 2.6–29.7 per cent. The source also showed a number of the 0.3–10 keV IDVs, sometimes observed within 1 ks observational runs. The X-ray flux mostly showed a correlated variability with the FACT excess rate, while few correlation was found with those from the optical-UV and HE γ-ray bands.

3.2 Spectral variability

Thanks to its unique characteristics, good photon statistics and the low background counts, *Swift*-XRT allows us to obtain high-quality spectra for the majority of the observations, derive the values of diverse spectral parameters and study their variability on time-scales as short as a few minutes for bright HBLs. According to the basic scenario, the X-ray emission is due to a synchrotron radiation from the highest energy electrons, and, therefore, a detailed spectral study in this band allows us to draw conclusions about the injection and radiative evolution of freshly accelerated particles (see Chiappetti et al. 1999, and references therein).

We performed the spectral analysis of the 0.3–10 keV spectra of Mrk 501 using the logparabolic model (LP; Massaro et al. 2004, hereafter M04):

$$F(E) = K(E/E_1)^{(-a+b\,\log(E/E_1))}\ \text{ph cm}^{-2}\ \text{s}^{-1}\ \text{keV}^{-1}, \quad (1)$$

where E_1 is the reference energy, generally fixed to 1 keV; a is the photon index at the energy E_1; b is the curvature parameter and K is the normalization factor. The values of these parameters are derived during the fit process. The position of the SED peak E_p and its height S_p are given by

$$E_p = E_1 10^{(2-a)/2b}, \quad (2)$$

$$S_p = 1.6 \times 10^{-9} K 10^{(2-a)^2/4b)}\ \text{erg cm}^{-2}\ \text{s}^{-1}. \quad (3)$$

We fixed the equivalent hydrogen column density to $N_H = 1.55 \times 10^{20}$ cm^{-2} from Kalberla et al. (2005). For each spectrum, the model validity was checked by means of reduced chi-square, distribution of the residuals and F-test. For the majority of the 0.3–10 keV spectra of Mrk 501, a single power law (see Section 3.2.3) was excluded at the 99.99 per cent confidence level or the LP model was clearly preferred by the aforementioned tests (for 154 out of 203 spectra). The corresponding results are provided in Table 5. For these spectra, a fit with the LP model showed better statistics than that with another logparabola model LPEP (Tramacere et al. 2009; hereafter T09)

$$F(E) = 1.6 \times 10^{-9} S_p 10^{-b(\log(E/E_p)^2)}\ \text{erg cm}^{-2}\ \text{s}^{-1}, \quad (4)$$

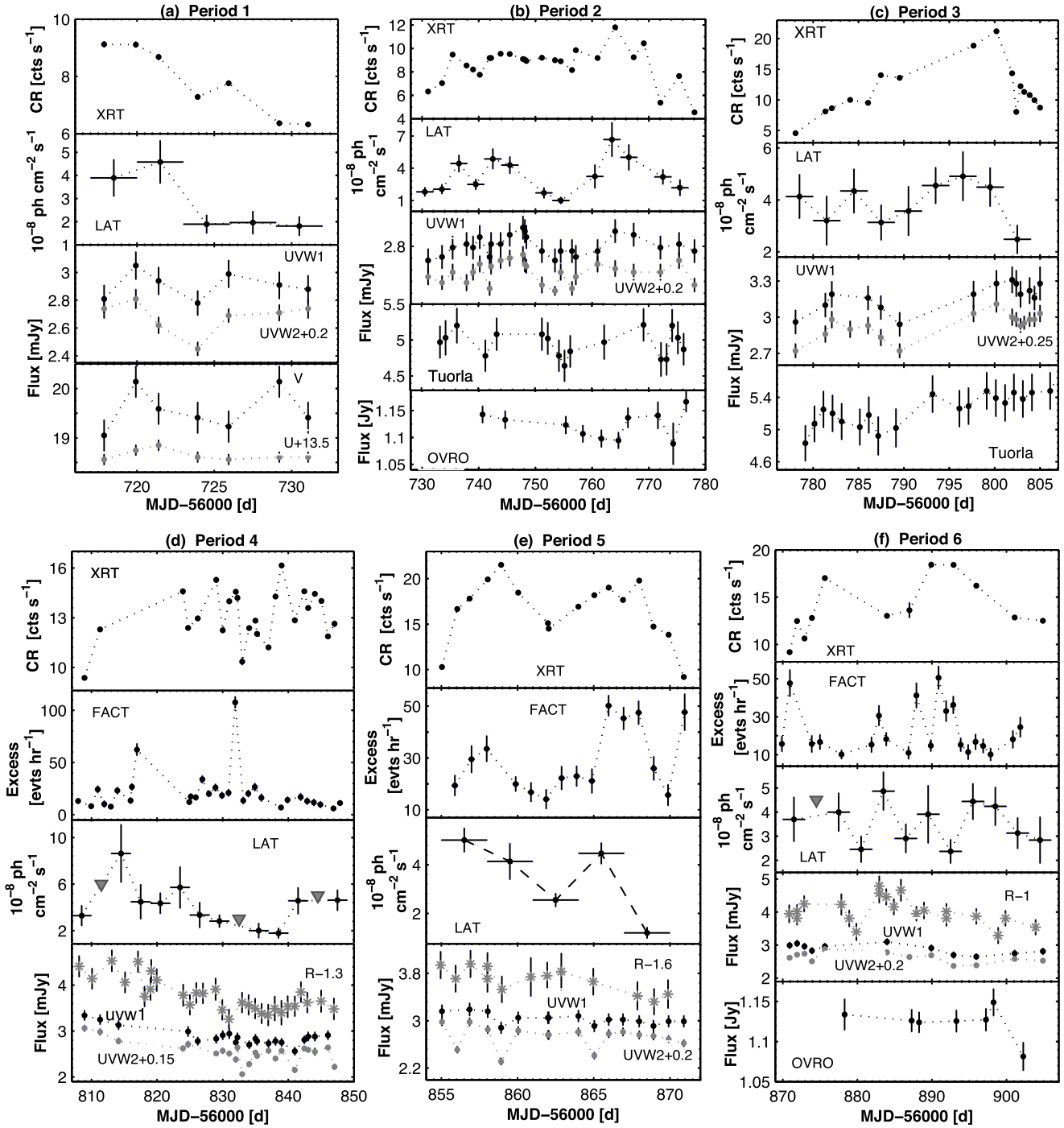

Figure 3. MWL variability of Mrk 501 in diverse epochs. The daily bins are used for the XRT, FACT, UVOT, Tuorla, OVRO light curves and the 3-d bins for the LAT data.

or a fit with a broken power law[8] (see Section 4.3.1, M04; T09; Perlman et al. 2005 for the physical reasons of the origin of log-parabolic spectra in BLLs).

Note that we have extracted the 0.3–10 keV spectra from separate orbits of a single observation when it was impossible to use the same source and background extraction regions for all orbits. The spectra were also obtained from the segments of one-orbit XRT observation when the source showed a flux variability during this observation, or none of the aforementioned models yielded satisfactory statistics when fitting the spectrum, extracted from the whole observation. In similar situations, we extracted the spectra even from the segments of the particular orbit. In Table 6, we present the properties of the distribution of diverse spectral parameters. The distribution peaks are derived via the lognormal fit to the corresponding histograms (Fig. 5).

[8] See https://heasarc.gsfc.nasa.gov/xanadu/xspec/manual/XSmodelBknpower.html

Table 4. Extract from the summary of IDVs at the 99.9 and 99.5 per cent confidence levels from the XRT observations of Mrk 501. Column 3 gives the total length of the particular observation (including the intervals between the separate orbits); Columns 7–9 present the ranges of the photon index at 1 keV, curvature parameter and the position of the synchrotron SED peak derived by means of the fit of the spectra, extracted from the separate orbits of the corresponding observation, with logparabolic or power-law spectral models.

ObsID(s)	Dates	Δt(h)	χ^2_r/d.o.f.	Bin (s)	F_{var}(per cent)	a or Γ	b	E_p (keV)
(1)	(2)	(3)	(4)	(5)	(6)	(7)	(8)	(9)
					99.9 per cent			
91745042, 3502300(8-9)	March 31–April 1	14.10	6.166/7	Orbit	4.4 (0.8)	1.81 (002)–1.90(0.03) (LP) 1.91(0.02)	0.09 (0.05)–0.22 (0.05)	2.58(0.39)–5.11 (0.45)
35023009	April 1	4.42	7.976/2	Orbit	2.6 (0.6)	1.81 (0.02)–1.83(0.02)	0.15 (0.04)–0.22(0.05)	2.43(0.26)–4.30(0.38)
35023020	May 4	1.08	2.719/18	60	7.4 (1.5)	1.69 (0.02)–1.77(0.03)	–	–

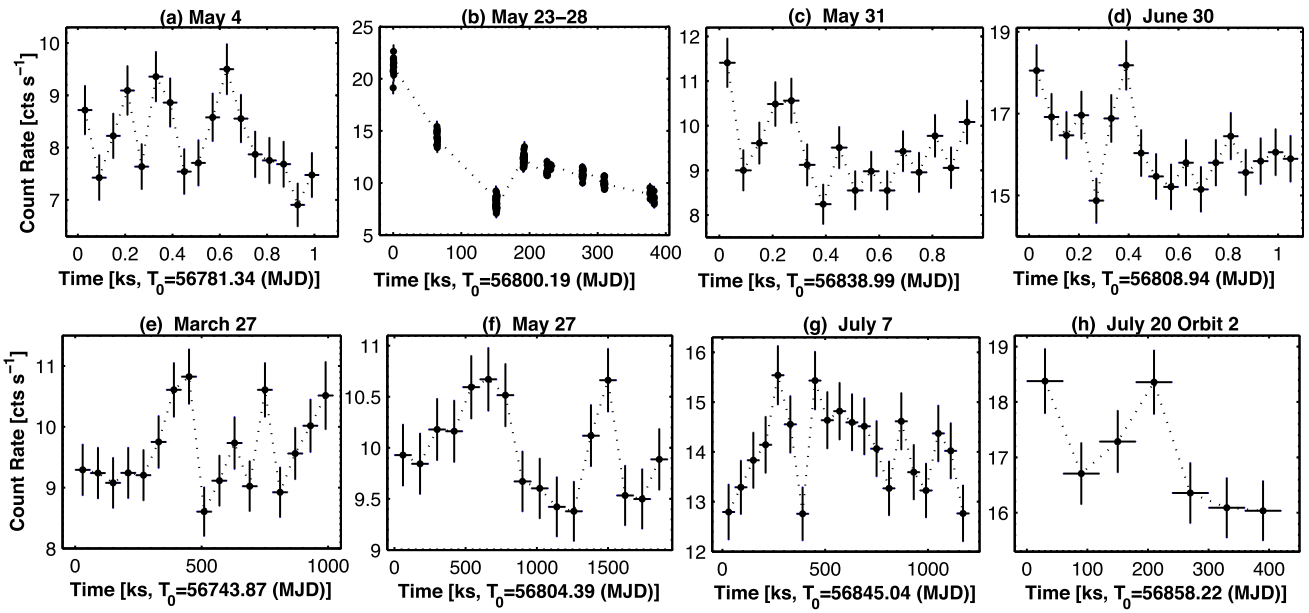

Figure 4. The most notable X-ray IDVs of Mrk 501 in 2014 March–October detected at the 99.9 per cent (top row) and 99.5 per cent (bottom row) confidence levels.

Table 5. Extract from the summary of the XRT spectral analysis with the LP. The E_p values (Column 4) are given in keV; unabsorbed 0.3–2, 2–10 and 0.3–10 keV fluxes (Columns 7–9) in erg cm^{-2} s^{-1}.

Obs Id	a	b	E_p	K	χ^2_r/d.o.f.	log $F_{0.3-2keV}$	log $F_{2-10keV}$	log$F_{0.3-10keV}$	HR
(1)	(2)	(3)	(4)	(5)	(6)	(7)	(8)	(9)	(10)
91745028 Part 1 (500 s)	1.83 (0.04)	0.15 (0.07)	3.69 (0.59)	0.0487 (0.0010)	0.929/153	−9.567 (0.009)	−9.863 (0.020)	−9.558 (0.011)	0.506 (0.025)
Part 2 (500 s)	1.82 (0.04)	0.13 (0.07)	4.92 (0.78)	0.0467 (0.0010)	0.996/99	−9.874 (0.010)	−9.858 (0.022)	−9.565 (0.012)	1.038 (0.058)
91745029 Part 1 (500 s)	1.85 (0.03)	0.16 (0.07)	2.94 (0.45)	0.0519 (0.0010)	0.930/161	−9.833 (0.009)	−9.825 (0.022)	−9.528 (0.012)	0.809 (0.044)

Table 6. Distribution of the spectral parameters.

Parameter	Minimum	Maximum	Peak	σ^2
a	1.39	2.02	1.69	0.015
b	0.13	0.53	0.23	0.048
E_p	0.79	20.96	3.45	16.71
Γ	1.54	1.98	1.77	0.014

3.2.1 Photon index

During 2014 March–October, the source often showed very hard spectra; the photon index at 1 keV ranged by $\Delta a = 0.63$ with the hardest value $a = 1.39 \pm 0.07$ derived from the first 500 s segment of ObsID 00035023074 (August 1, MJD 56870.9; see the corresponding spectrum in the logν–νF_ν representation in Fig. 6), and the 153 out of 154 curved spectra were harder than $a = 2.00$ (see Fig. 5a). The photon index is almost symmetrically distributed with respect to the peak value $a_{max} = 1.69$, and their 18.2 per cent are harder than $a = 1.60$ that is uncommon for BLLs. The mean value of these parameters in different periods (discussed in Section 3.1) showed a range $\overline{a} = 1.59$–1.90. The 'softest' spectra with $\overline{a} = 1.86$–1.90 belong to the epoch of Periods 1–2, while the hardest spectra are derived from the observations performed in Period 5. The spectra with $a < 1.69$ generally correspond to the unabsorbed 0.3–10 keV flux values larger than $\overline{F}_{0.3-10\,keV} = (3.53 \pm 0.07) \times 10^{-10}$ erg cm^{-2} s^{-1} that is the weighted mean unabsorbed flux value during 2014 March–October, while the softer spectra are characterized by the fluxes below this threshold. This means that the source mostly followed a 'harder-when-brighter' trend in the here presented period that is reflected in Fig. 7a, exhibiting an

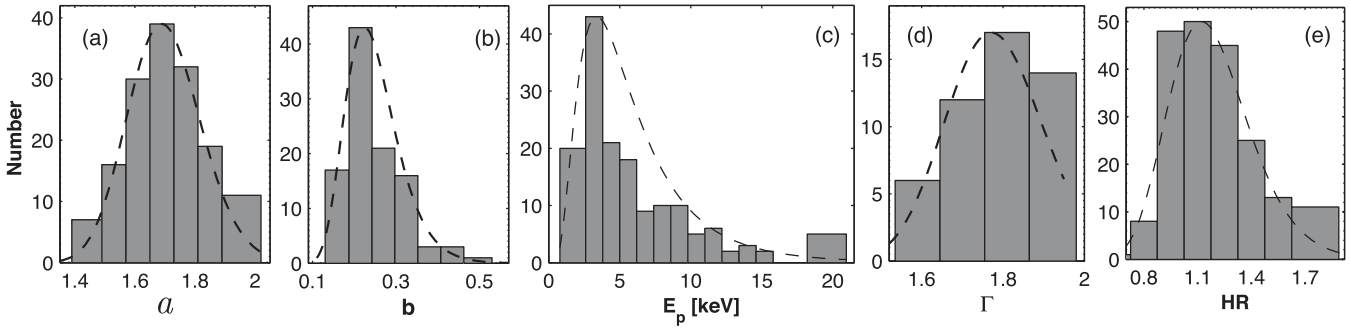

Figure 5. Distribution of the values of diverse spectral parameters (photon index at 1 keV, curvature parameter, position of the SED peak and photon index throughout the 0.3–10 keV energy range) and HR. The dashed lines represent the lognormal fit to the distributions.

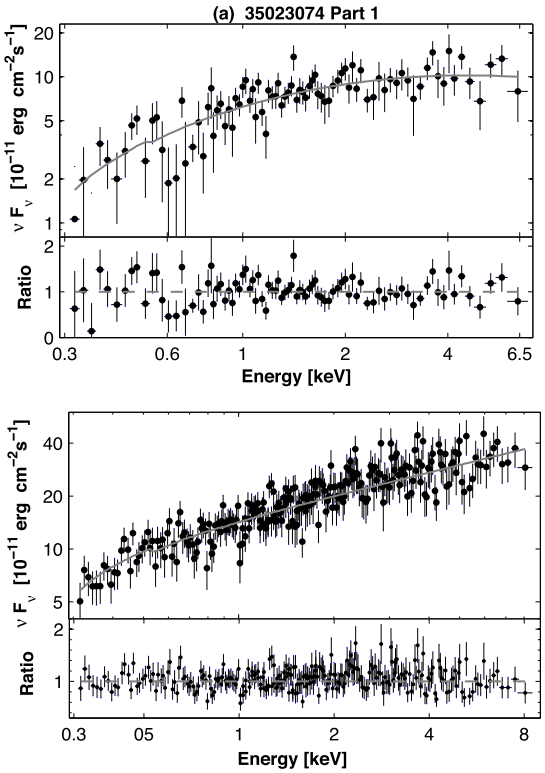

Figure 6. The hardest 0.3–10 keV spectra of Mrk 501 from the 2014 March–October period fitted with the LP (top plot) and PL (bottom plot) models. The first spectrum corresponds to the first 500 s segment of the August 1 observation (ObsID 00035023074, MJD 56870.9) yielding $a = 1.39 \pm 0.06$, $b = 0.46 \pm 0.13$ and $\chi^2_r = 1.024$ with 84 d.o.f. The PL spectrum is extracted from the second 500 s segment of the May 20 observation (MJD 56797.7) with $\Gamma = 1.54 \pm 0.02$, $\chi^2_r = 0.950$ with 254 d.o.f.

anticorrelation between the parameter a and the 0.3–10 keV flux (see Table 7 for the corresponding Pearson coefficient r and p chances). Note that the 'harder-when-brighter' trend was absent with no significant correlation between a and $F_{0.3-10\,\mathrm{keV}}$ in Periods 2 and 5.

A 'harder-when-brighter' behaviour of the source is more evident from Fig. 8b that shows a timing of the parameter a along with the unabsorbed 0.3–2 and 2–10 keV fluxes. We see that the photon index varied on different time-scales (see also Fig. 9, online material). The largest variability was recorded in Period 3 where the photon index hardened by $\Delta a = 0.35$ in 19 d, followed by a softening by $\Delta a = 0.37$ in 6 d (Fig. 9c). The fastest softening by $\Delta a = 0.36$ in 2 d was recorded in the beginning of Period 5 (Fig. 9f), and the 0.3–10 keV spectrum hardened by $\Delta a = 0.25$ in the same time in Period 4 (between MJD 56837 and MJD 56839; see Fig. 9d). On intraday time-scales, the parameter a showed the fastest hardening by $\Delta a = 0.13 \pm 0.04$ in 5.8 h (June 17, MJD 56824.7; see Table 4).

3.2.2 *Spectral curvature and the position of the synchrotron SED peak*

Although the curvature parameter showed a wide range between $b = 0.09 \pm 0.04$ and 0.53 ± 0.10, its values were relatively small, and only 9 out of the 154 curved spectra yield $b > 0.35$ (see Fig. 5b). They were mostly included in the interval $b = 0.15-03.30$ (72 per cent). The mean value of the curvature parameter from each period ranged between $\overline{b} = 0.13$ (Period 1) and $\overline{b} = 0.24$ (Periods 4–5). This parameter showed a weak anticorrelation with E_p (Fig. 7b), which is expected in the framework of some acceleration mechanisms (see Section 4.3.1 for the corresponding discussion). As for the timing of the curvature parameter, it showed a variability with 3σ significance ($\chi^2_r = 1.45$ with 153 d.o.f.) but did not exhibit any clear trend during the whole March–October period (Fig. 8d).

The parameter E_p showed an extremely large range from 0.79 ± 0.08 to 20.96 ± 2.81 keV and the distribution peak at 3.45 keV (see Fig. 5c). The position of the SED peak was found only seven times below $E = 2$ keV (the dividing line between the soft and hard X-rays), and they all belong to Periods 1–2. In the case of 21 spectra, $E_\mathrm{p} > 10$ keV and these values can be considered as upper limits to the intrinsic position the synchrotron SED, peak since they are not covered by the instrumental range.

This parameter shows a positive correlation with the 0.3–10 keV flux (Fig. 7c) that is also evident from Fig. 8e, where we observe the five consecutive peaks. The first four peaks coincide with the peaks of the 0.3–2 and 2–10 keV fluxes (see Fig. 8a). The position of the SED peak shifted by 5.5–17.1 keV towards higher energies with an increasing flux in the epochs of short-term X-ray flares, and moved back to lower energies as source become progressively fainter (see also Fig. 9, online material). The last peak in Fig. 8e makes some exclusion from the general trend where there is fast increase by 16.8 keV till 20.32 ± keV in about 1.2 d in the epoch of a decreasing flux. Note that we do not observe a significant E_p–flux correlation in Periods 2 and 5, similar to the a–flux case.

3.2.3 *Power-law spectra*

49 spectra out of 203 did not show a significant curvature, and their fit with the LP model did not yield better statistics than a simple power-law model, given by $F(E) = KE^{-\Gamma}$, where Γ is the photon

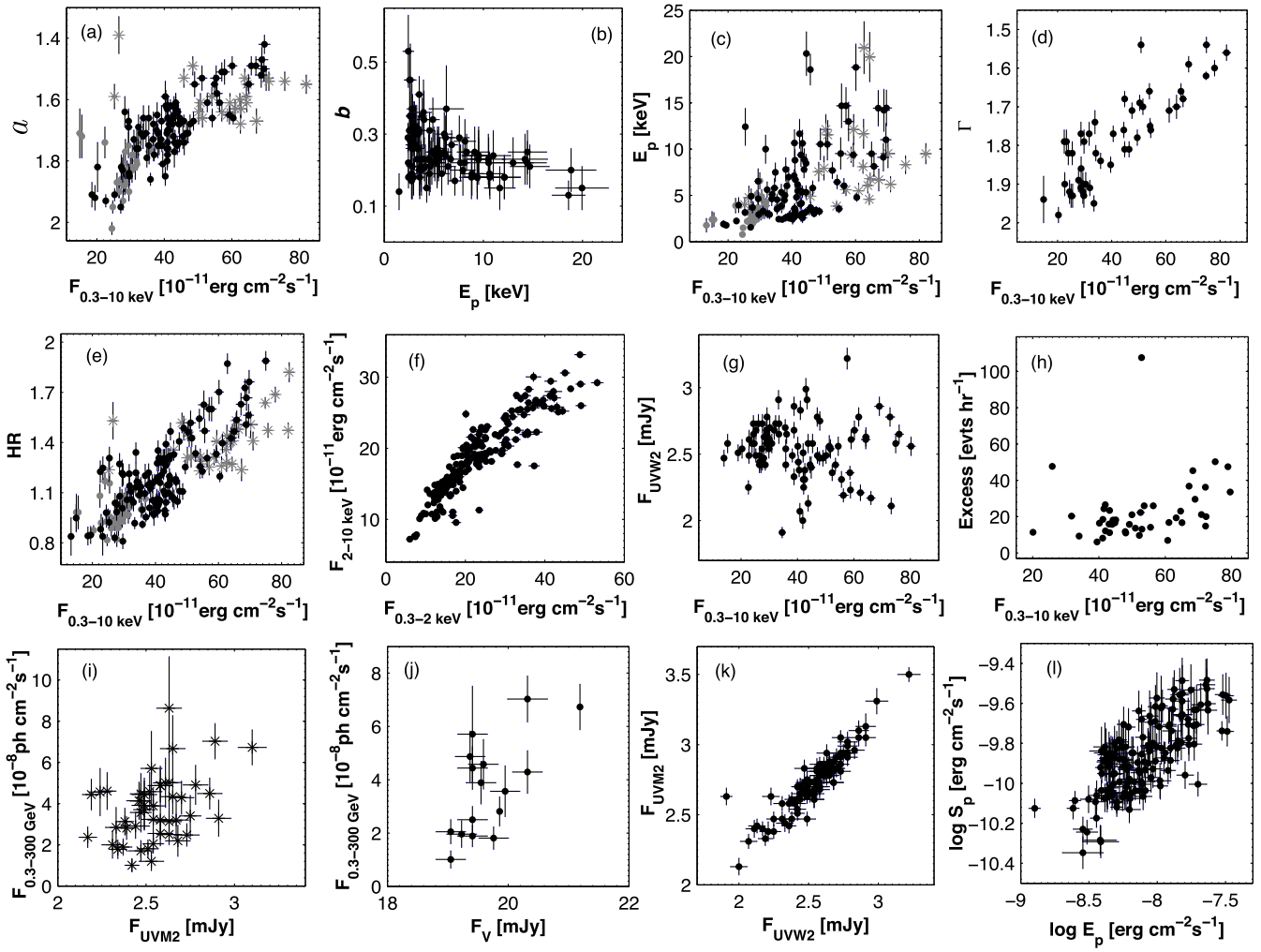

Figure 7. Correlation between different spectral parameters and fluxes (denoted by 'F_i' for the particular i band). In the panels (a), (c) and (e), the data from Periods 2 and 5 are plotted with grey points and asterisks, respectively.

index throughout the observation band, and the units of the normalization factor K are photons cm^{-2} s^{-1} keV^{-1}. Therefore, we chose the latter model for these spectra (see Table 8 for the results). Note that the broad-band SEDs constructed for those observation show the presence of the synchrotron peak in the aforementioned range of the parameter $E_{\rm p}$, and the better statistics for the PL fit compared to the LP one cannot be related to presence of the synchrotron SED peak far from the instrumental range of the XRT that, on its turn, makes difficult to evaluate a possible curvature, and a simple power-law model gives a relatively better description of the spectrum (see Massaro et al. 2008, k14). These spectra generally are also hard with the range $\Delta\Gamma = 0.54$ and the hardest spectrum corresponding to $\Gamma = 1.54 \pm 0.02$ (see Fig. 5d for the distribution of the photon index and Fig. 6 for the hardest PL spectrum). The LP spectra are found in all periods, in any brightness state of the source, and they exhibit a 'harder-when-brighter' spectral evolution stronger than do the LP spectra (see Fig. 7d and Table 7). Note that some observations showed the presence of both LP and PL spectra, extracted from its different segments or orbits. The most remarkable example is the XRT observation performed on May 25 (MJD 56802.85) when the first, second and fourth 500-s segments show LP spectra [yielding $a = 1.65$ (0.04)–1.73 (0.03), $b = 0.16$ (0.07)–0.25 (0.07), $\chi^2_{\rm r} = 0.935$–0.996 with 197–202 d.o.f.], while that from the third segment fits well with the PL model ($\Gamma = 1.77 \pm 0.02$, $\chi^2_{\rm r} = 1.004$ with 254 d.o.f.). Similar to the photon index at 1 keV, the parameter Γ varied with $\Delta\Gamma = 0.19$–0.41 on diverse time-scales, and the fastest variability was a hardening by $\Delta\Gamma = 0.13$ within 17.3 h (recorded on MJD 56781).

Note also that the source generally showed power-law 0.3–300 GeV spectra from the 3-d binned LAT observations in the period presented here, which often were very hard: more than 50 per cent of them showed the photon index $\Gamma < 1.70$ down to $\Gamma = 1.28 \pm 0.14$.

Table 7. Correlations between spectral parameters and multiband fluxes (denoted by 'F_i' for the particular i band).

Quantities	r	p
a and $F_{0.3-10\,\rm keV}$	−0.62 (0.07)	3.82×10^{-10}
a and $F_{2-10\,\rm keV}$	−0.67 (0.06)	4.24×10^{-11}
b and $E_{\rm p}$	−0.35 (0.10)	4.42×10^{-5}
$E_{\rm p}$ and $F_{0.3-10\,\rm keV}$	0.48 (0.09)	3.57×10^{-7}
$E_{\rm p}$ and $F_{2-10\,\rm keV}$	0.53 (0.08)	6.11×10^{-8}
Γ and $F_{0.3-10\,\rm keV}$	−0.77 (0.05)	8.88×10^{-12}
Γ and $F_{2-10\,\rm keV}$	−0.80 (0.04)	4.05×10^{-13}
$\log E_{\rm p}$ and $\log S_{\rm p}$	0.66 (0.09)	5.35×10^{-10}

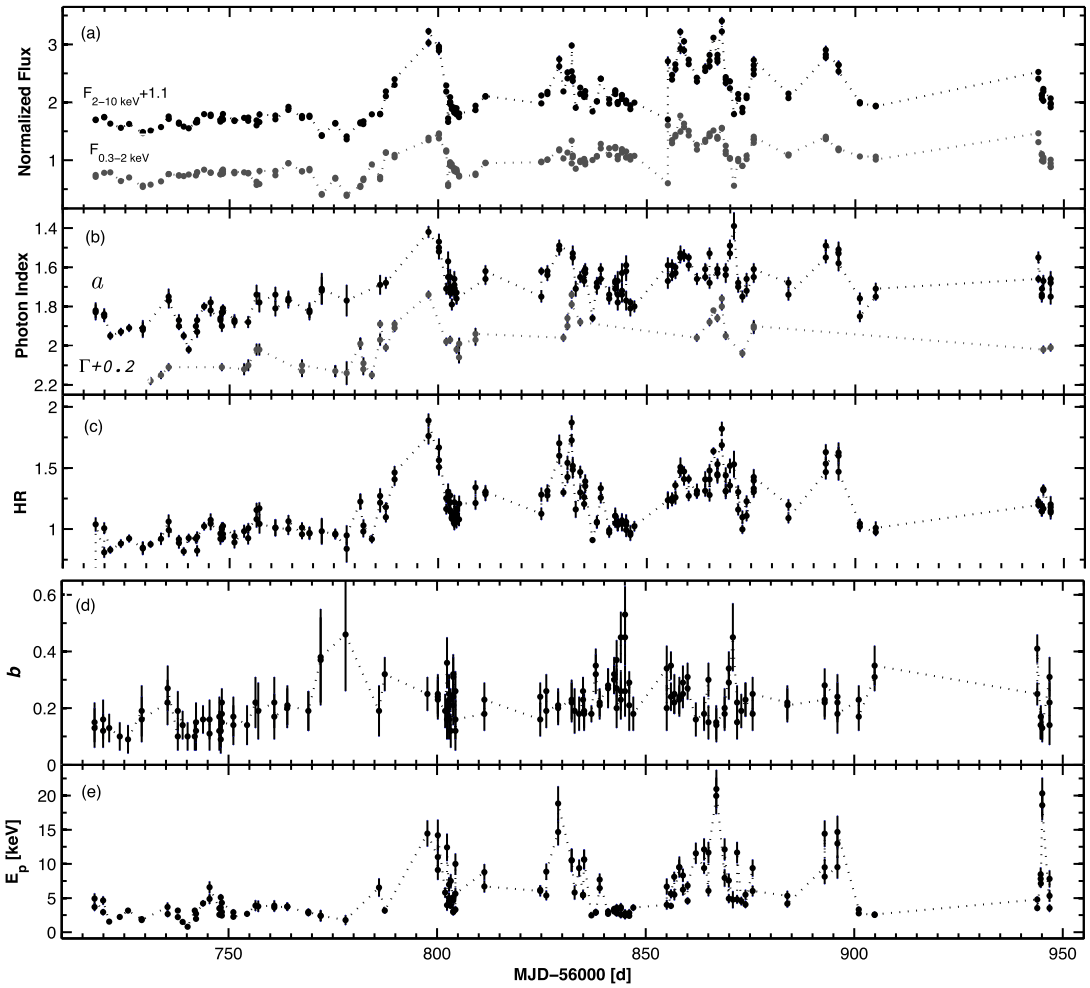

Figure 8. Unabsorbed 0.3–2 and 2–10 keV model fluxes normalized to their mean values in the period 2014 March–October (top panel; the 2–10 keV plot is shifted arbitrarily for a better resolution), photon index (panel b), HR (panel c), curvature parameter (panel d) and E_p (bottom panel) plotted versus time.

Our spectral study shows that the majority of the 0.3–10 keV spectra of Mrk 501 were curved and described by the logparabola model well with broad ranges of photon index, hardness ratio (HR) and synchrotron SED peak location. High brightness states and strong fast intraday variability of the 0.3–2 and 2–10 keV fluxes, which was stronger towards higher frequencies, allowed us to detect very fast spectral variability. Namely, a hardening by $\Delta a = 0.13$ in 6 h, increase and decline of the parameter E_p by 16.8 keV in 1.2 and 1.7 d, respectively, are the fastest spectral variability events reported for this source to date (found by us in this study). The spectral parameters varied on different time-scales, and the source exhibited a 'harder-when-brighter' spectral evolution with the flux variability.

3.3 HR and spectral hysteresis

The HR, corresponding to each 0.3–10 keV spectrum of Mrk 501, was calculated as a ratio of unabsorbed 2–10 to 0.3–2 keV flux derived from the particular spectrum. This quantity confirms the presence of the aforementioned 'harder-when-brighter' trend (see Fig. 7e and Table 9), and it shows a wide range $\Delta\mathrm{HR} = 1.079$ and $\mathrm{HR_{max}} = 1.888$ (Fig. 5e, including the values derived from the spectra fitted with the power-law model). The 76.6 per cent of all spectra are characterized by $\mathrm{HR} \geq 1.00$, and the mean value of this parameter from each period, discussed in Section 3.1.3, ranged from $\overline{\mathrm{HR}} = 0.890$ (Period 1) to $\overline{\mathrm{HR}} = 1.414$ (Period 5). Similar to the photon index, the HR was not correlated with the 0.3–10 keV flux in Periods 2 and 5, and the corresponding data points produce outliers

Table 8. Extract from the summary of the XRT spectral analysis with a simple PL model. Unabsorbed 0.3–2, 2–10 and 0.3–10 keV fluxes (Columns 5–7) are given in erg $\mathrm{cm^{-2}\ s^{-1}}$.

ObsId (1)	Γ (2)	K (3)	χ^2_r/d.o.f. (4)	$\log F_{0.3-2\,\mathrm{keV}}$ (5)	$\log F_{2-10\,\mathrm{keV}}$ (6)	$\log F_{0.3-10\,\mathrm{keV}}$ (7)	HR (8)
00091745035	1.98 (0.02)	0.0359 (0.0005)	1.009/195	−9.964 (0.007)	−10.022 (0.012)	−9.691 (0.006)	0.875 (0.028)
00091745036 Part 1 (500 s)	1.90 (0.03)	0.0381 (0.0008)	0.926/129	−9.947 (0.010)	−9.629 (0.017)	−9.645 (0.009)	1.807 (0.082)
00091745037	1.91 (0.02)	0.0538 (0.0006)	1.056/228	−9.796 (0.006)	−9.798 (0.010)	−9.496 (0.006)	0.995 (0.027)

Table 9. Correlations between the model-independent quantities ('F_i' stands for the flux in the particular i band).

Quantities	r	p
HR and $F_{0.3-10\,\mathrm{keV}}$	0.64 (0.06)	1.54×10^{-11}
HR and $F_{2-10\,\mathrm{keV}}$	0.71 (0.04)	5.35×10^{-12}
$F_{0.3-2\,\mathrm{keV}}$ and $F_{2-10\,\mathrm{keV}}$	0.85 (0.03)	$<10^{-15}$
$F_{0.3-10\,\mathrm{keV}}$ and F_{FACT}	0.59 (0.09)	2.10×10^{-8}
F_{UVW2} and F_{UVM2}	0.87 (0.03)	$<10^{-15}$
F_{UVW2} and F_{UVW1}	0.88 (0.03)	$<10^{-15}$
F_{UVW2} and F_{U}	0.86 (0.03)	$<10^{-15}$
F_{UVW2} and F_{B}	0.71 (0.05)	8.10×10^{-12}
F_{UVW2} and F_{V}	0.62 (0.07)	1.07×10^{-10}
F_{UVM2} and F_{UVW1}	0.90 (0.02)	$<10^{-15}$
F_{UVM2} and F_{U}	0.87 (0.03)	$<10^{-15}$
F_{UVM2} and F_{B}	0.73 (0.05)	2.02×10^{-13}
F_{UVM2} and F_{V}	0.67 (0.06)	9.26×10^{-11}
F_{UVW1} and F_{U}	0.87 (0.03)	$<10^{-15}$
F_{UVW1} and F_{B}	0.74 (0.05)	1.19×10^{-13}
F_{UVW1} and F_{V}	0.68 (0.06)	4.57×10^{-12}
F_{U} and F_{B}	0.75 (0.05)	8.65×10^{-13}
F_{U} and F_{V}	0.66 (0.06)	3.78×10^{-11}
F_{B} and F_{V}	0.52 (0.10)	7.92×10^{-8}
F_{UVW2} and $F_{0.3-300\,\mathrm{GeV}}$	0.33 (0.12)	1.92×10^{-4}
F_{UVM2} and $F_{0.3-300\,\mathrm{GeV}}$	0.38 (0.11)	4.15×10^{-5}
F_{UVW1} and $F_{0.3-300\,\mathrm{GeV}}$	0.36 (0.11)	6.76×10^{-4}
F_{U} and $F_{0.3-300\,\mathrm{GeV}}$	0.56 (0.10)	2.34×10^{-6}
F_{V} and $F_{0.3-300\,\mathrm{GeV}}$	0.50 (0.11)	3.11×10^{-5}
F_{U} and $F_{0.3-300\,\mathrm{GeV}}$	0.54 (0.11)	8.40×10^{-5}

from the general trend in Fig. 7e. This parameter also showed a variability on various time-scales (Figs 8c and 9a–f).

We constructed an HR – 0.3–10 keV flux plane (see Section 4.4 for its physical implication) for each period (Fig. 10). In the case of Periods 1–5, we split this plane into two parts for a better resolution. In this plane, the source exhibited a complex behaviour, and its spectral evolution followed a clockwise (CW) or a counterclockwise (CCW) loops during the short-term X-ray flares presented in Section 3.1.3, or showed a change from a CW loop into the opposite one and vice versa within a single flare.

Namely, the source followed a CW loop during the initial, relatively short part of Periods 2 and 6, then it changed into CCW loops that lasted significantly longer (Figs 10a and c, respectively). In Period 5, the first 'hump' showed a CCW-type evolution, while we observe an opposite trend for the second one that lasted twice longer than the first 'hump'. In contrast, we observe a CCW-type evolution in the initial rising part of the strongest short-term flare during 2014 March–October (Period 3), and the next rising and decaying parts of this flare and the subsequent minor flare were characterized by CW loops (Fig. 10b). As noted in Section 3.1.3, this strong flare established the highest historical brightness state of Mrk 501, and there is a possible soft lag in the flare maximum epoch (see the third panel of Fig. 10b): the hard flux peaked on MJD 56797.7, while the largest soft flux was observed with the 2.5-d delay. However, we cannot use the local cross-correlation function (Max-Moerbeck et al. 2014) and derive the value of a hard lag, since the duration of each observation generally was much shorter than the time intervals between them.

The situation was more complex in Period 4 when the source initially exhibited a CW-type hysteresis that lasted about a half of this period (Fig. 10c). Then it followed a CCW loop during the fast and smaller-amplitude flare with a possible hard lag: the 0.3-keV peak was observed on MJD 56830.998 while the hard one peaked on MJD 56332.004. The next two fast, low-amplitude flares between MJD 56832.98 and 56841 show a CW trend and the hard peak is recorded by 22.5 h earlier than the soft one. Finally, the source exhibited CCW loop during the fluctuations observed during the last 6 d of this period. A pure CW loop is revealed only for the IDV recorded on May 25–26 [ObsIDs 000350230(30–31), MJD 56803] that show a lagged soft X-ray light variability: we observed a peak in the light curve after 1.25 ± 0.25 ks since the start ObsID 00035023030, while a hard peak was not recorded during this pointing (see Fig. 10f).

4 DISCUSSION

In this section, we discuss the results from the MWL flux variability and X-ray spectral study of Mrk 501 along with those published to date.

4.1 Flux variability

4.1.1 Variability amplitudes

During the period 2014 March–October, Mrk 501 varied by a factor of 4.7 and 0.3–10 keV count rate attained to the value of 21.2 cts s^{-1}, making our target one of the brightest sources in the X-ray sky. As for the whole set of the XRT observations of Mrk 501 since 2005, the maximum-to-minimum flux ratio $R = 7.46$, which is a modest value compared to Mrk 421 ($R = 22$ only for the period 2013 January–May; Kapanadze et al. 2016c), PKS 2155−304 ($R = 24$ in 2005–2012; Kapanadze et al. 2014) and 1ES 1959+650 ($R = 13.34$ in 2005–2015; Kapanadze et al. 2016a,b). As for the past X-ray observations performed with other space missions, the source showed the ratio R amounting to 12.0–21.3 during the *RXTE*-ASM and *RXTE*-PCA observations in 1996–1999 (Xue & Cui 2005). It underwent more extreme variability in the VHE band, boosting by a factor 20 during the 6 d observations with HEGRA in 1997 April (Sambruna et al. 2000), and the MAGIC observations showed a variability by a factor of 23, including a flare by a factor of 4 in 4 d during 2013 April–August (Furniss et al. 2015).

The flux variability of Mrk 501 shows a double-peaked shape with the highest variability in the X-ray and VHE bands in Fig. 11 a where the F_{var} values from each band, calculated using all the available data obtained during the 2014 March–October period with various instruments, are plotted versus frequency. The value of F_{var} is known to be dependent on the data sampling, and it should be interpreted with a caution. Note also that the F_{var} values derived from the optical UVOT and Steward Observatory data can be underestimated since the host contribution is not subtracted. Generally, F_{var} was derived using the individual single-day measurements of Mrk 501, except for BAT and LAT, for which, because of the limited sensitivity, we used data integrated over one week and 3 d, respectively. Although a limited sensitivity and the use of larger time bins can underestimate F_{var} values for these instruments, a double-peak shape in the F_{var}–logν plane is inherent for HBLs, and it has been reported by various authors. Namely, a similar shape of F_{var} with frequency was reported for Mrk 421 from the MWL campaigns performed various epochs (Aleksic et al. 2015c; Balokovic et al. 2016; Kapanadze et al. 2016c), 1ES 1959+650 in 2005–2014 (Kapanadze et al. 2016a), etc. This shape with the highest variability in the X-ray and VHE bands was interpreted as resulting from a correlation between the synchrotron and IC peaks by Furniss et al. (2015), and as an indication that the electron energy distribution is most variable at the highest energies (within the one-zone SSC scenario; see Aleksic et al. 2015c). Note that a double-peak shape is evident

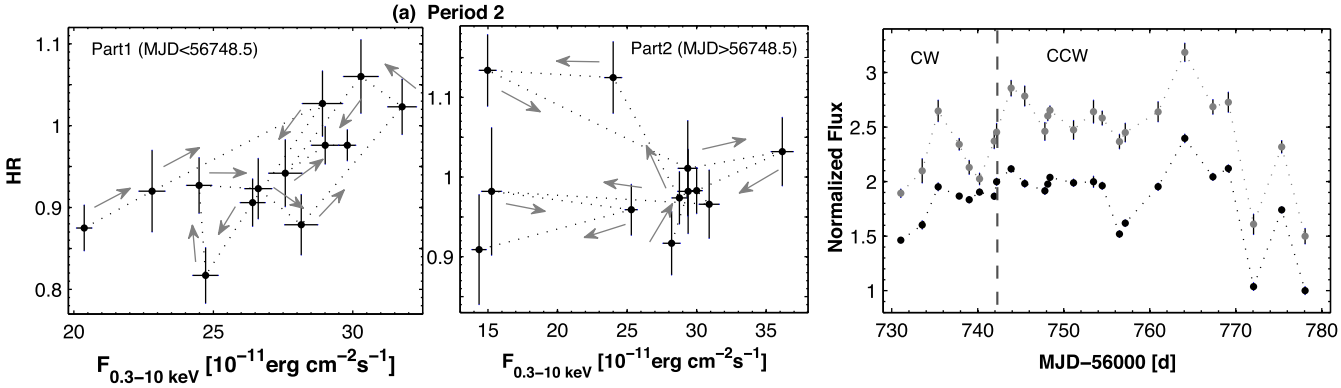

Figure 10. Spectral hysteresis in different epochs with the soft 0.3–2 keV (black points) and hard 2–10 keV (grey points) fluxes plotted versus time (extract). The light curves for hard fluxes are shifted arbitrarily for a better resolution.

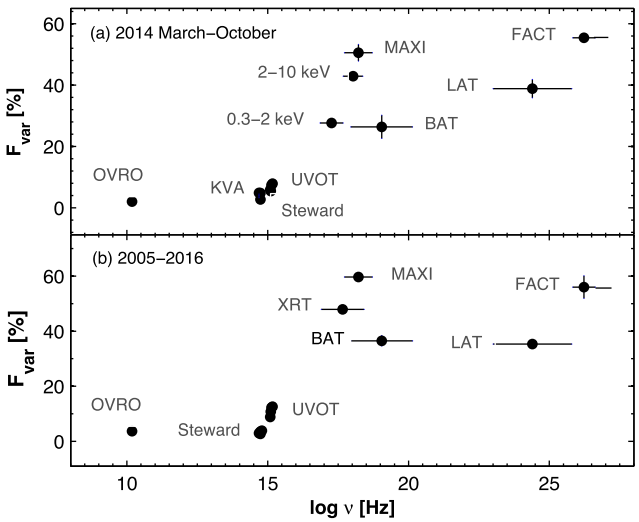

Figure 11. Fractional rms variability amplitude as a function of the energy for the periods 2014 March–October (top panel) and 2005–2016 (bottom panel).

from Fig. 11b, where a F_{var}–logν plane is constructed for Mrk 501 using the MWL data from the whole 2005–2016 period.

4.1.2 Intraday variability

The duty cycle (DC, i.e. the fraction of total observation time during which the object displays a variability) of the 0.3–10 keV IDVs, detected for our target at the 99.5 per cent confidence level during 2014 March–October, is 51.5 per cent, and this parameter attains 55.6 per cent including the IDVs, detected at the 99.5 per cent confidence level. PKS 2155−304 showed a comparable DC (48 per cent; K14) during the XRT observations in 2005–2012. As for 1ES 1959+650, it showed a significantly smaller DC during the XRT campaigns performed in the periods 2005–2014 (28.2 per cent; K16a) and 2015 August–2016 January (28.1 per cent; K16b). However, this source showed DC = 52.5 per cent in 2016 January–August (Kapanadze et al., in preparation) when the XRT observations were more densely sampled than in 2015 August–2016 January, and it often was observed twice a day, similar to Mrk 501 in the period presented here. On the other hand, our target was less variable on intranight time-scales in the X-ray band than Mrk 421 in 2013 January–May when the DC amounted to 83 and 99 per cent for the XRT and *NuSTAR* observations, respectively (Kapanadze et al. 2016c).

From the past X-ray observations of Mrk 501, an extreme IDV was reported by Catanese & Sambruna (2000) when an increase of the 2–10 keV flux by 60 per cent in 200 s was followed by a drop by 40 per cent in 600 s from the *RXTE*-PCA observation on 1998 May 25. However, this detection was attributed to the instrumental effects by Xue & Cui (2005). Note that Mrk 501 showed more extreme IDVs in the VHE band. Namely, at the peak of the TeV flare in 1998 June, the flux doubled in about 20 min (Sambruna et al. 2000). The HEGRA observations revealed an increase by a factor of 4.3 on 1997 April 12 (Aharonian et al. 1999). The most extreme variability with flux-doubling times down to 2 min was reported by Albert et al. (2007) from the MAGIC observation on 2005 June 30 and 9. Finally, the source showed a flux-doubling time shorter than 10 min from the HESS observations of 2014 June 23–24 (Chakraborty et al. 2015).

It is important to check an occurrence of IDVs in various brightness states, which can hint at the possible origin of these fast variability events. Namely, the IDVs observed during flaring epochs are in favour of the shock-in-jet scenario (interaction of a propagating shock front with the jet inhomogeneities; Sokolov, Marscher & McHardy 2004), while those caused by other instability mechanisms occurring near the event horizon of central black hole should be more conspicuous when the source is faint (see e.g. Mangalam & Wiita 1993; Kapanadze 2009). In that case, the variable emission from the black hole vicinity will not be 'shadowed' by the huge amount of the flux generated by the emission zone following the shock front that propagates towards the observer. Similar to 1ES 1959+650 and Mrk 421 (see Kapanadze et al. 2016a,c), the majority of the 0.3–10 keV IDVs in Mrk 501 (65 per cent) were observed in higher brightness states and fractional variability amplitudes of IDVs showed largest values for lower brightness states, while the brightest states were characterized by smallest F_{var} values. However, an anticorrelation between F_{var} and $F_{0.3-10\,keV}$ was not statistically significant ($r = 0.28$, $p = 0.052$) for Mrk 501, in contrast to the aforementioned two sources. Furthermore, our target showed different levels of the activity on intraday time-scales during 2014 March–October: there were the epochs with enhanced activity and the epochs when the source was relatively passive (even in the case of densely sampled XRT observations). Note that Mrk 501 did not exhibit an intraday activity during some past X-ray campaigns, e.g. the 2.5-d *ROSAT* observation performed in 1991 August did not show a significant variability in the 0.1–2.4 keV band (Fink et al. 1991).

4.2 Interband cross-correlations

4.2.1 Soft and hard X-rays

The unabsorbed soft 0.3–2 keV flux showed a strong positive correlation with the hard 2–10 keV flux (see Figs 7f and 8a). In each period, the corresponding light curves followed each other closely. However, the hard flux varied by a larger amplitude than the soft one in each period (see Table 3), leading to the strong spectral variability. This difference was especially large in Period 3 when the 0.3–2 keV flux varied by a factor of 3.8, while we observe a variability by a factor 8.2 in the 2–10 keV band. Note that the weighted mean hard X-ray flux for the whole March–October period was larger than the soft one (1.82 ± 0.01 versus 1.73 ± 0.01, in units of 10^{-10} erg cm^{-2} s^{-1}) and 76 per cent of the spectra show larger hard flux than the soft one that is uncommon for BLLs. Note that the maximum 2–10 keV flux from this period $F^{\rm max}_{2-10{\rm keV}} = (5.32 \pm 0.15) \times 10^{-10}$ erg cm^{-2} s^{-1} is practically equal to the previous highest historical value from the prominent 1997 April 16 observation with $E_{\rm p} \sim 100$ keV (5.24×10^{-10} erg cm^{-2} s^{-1}; M08).

4.2.2 X-ray–TeV correlation

In Periods 4–6 (when the source was detected frequently by FACT), X-ray flares generally were accompanied by their TeV counterparts, resulting in a moderate positive correlation between the data sets of the simultaneous XRT and FACT observations (see Fig. 7h and Table 9), if we remove the FACT observations performed on MJD 56831 and MJD 56871 (discussed in Section 3.1.3 and producing outliers from the general trend in Fig. 7h) from the scatter plot. During the past MWL campaigns, a correlated TeV–X-ray variability was observed in 1997 April (Pian et al. 1998), 2004 June (Gliozzi et al. 2006), 2008 March–May (Aleksic et al. 2015a), 2011 May (Shukla et al. 2015), 2013 April–August (Furniss et al. 2015) and the correlation was stronger with increasing brightness states. However, we have also revealed an uncorrelated variability of XRT and FACT fluxes during MJD 56873–56875 when the 0.3–10 keV flux showed an increase by 85 per cent, while the source did not show TeV-band variations in this time interval and exhibited its low TeV state. However, the FACT observations showed a fast flare about 2 d earlier (the first, lower outlier in Fig. 7h). Such shifted X-ray-TeV flaring behaviour poses a challenge to one-zone SSC models. A very strong, fast TeV flare by a factor of 5.1 on MJD 56831 (Period 4; the second, higher outlier in Fig. 7h) was accompanied by an increase in the X-ray flux only by 19 per cent which is also a challenge for these models. Similarly, Mrk 501 underwent a TeV flare by a factor of 5 during MJD 54953–54956 in 2009 (Abdo et al. 2011) while only a modest increase (by 60 per cent) in the X-ray brightness was recorded with the simultaneous XRT observations.

4.2.3 X-ray versus GeV-band and optical-UV variability

The 0.3–10 keV flux mostly showed an uncorrelated behaviour with the LAT-band and optical-UV fluxes, while there is a positive correlation between the 0.3–300 GeV and UVOT-band fluxes. Namely, the LAT-band flux showed weak correlations with those from the *UVW1, UVMM2, UVW1*-band fluxes with $r = 0.33$–0.38, and it exhibited a stronger connection with the *U-, B-, V*-band fluxes, yielding a moderate correlation with $r = 0.50$–0.56 (see Figs 7i–7j). This result can be explained by the stronger connection between the optical-UV and HE γ-ray emissions via the IC scatter of synchrotron photons, while the contribution of X-ray photons to the 0.3–300 GeV band should be significantly smaller for Mrk 501 in the here presented period. T09 suggested a possibility of a positive correlation between the UV and MeV/GeV-band fluxes via the effect of the Klein–Nishina suppression in the IC process, leading to the UV photons being upscattered most efficiently at the GeV energies by the electrons radiating in the X-ray.

For Mrk 501, a lack or absence of the correlated variability of the X-ray flux with the HE and optical-UV fluxes was reported also by Bartoli et al. (2012) and Furniss et al. (2015). A similar result was reported for Mrk 421 by Kapanadze et al. (2016c), Balokovic et al. (2016) and Bartoli et al. (2016). During the MWL campaign in 2009 January–June for this source, Aleksic et al. (2015b) observed an overall anticorrelation between optical/UV and X-rays, and explained it via the hardening in the electron energy distribution that can shift the entire synchrotron bump to higher energies: if the spectral index of the electron population is getting harder, the emission at the rising segment of the synchrotron SED (radio–UV) will decline, while that on the decreasing segment (X-rays) increases. A trend of decreasing optical-UV fluxes with rising X-ray brightness was also observed for our target in Periods 4–6, and these occasions can be also explained by means the scenario proposed by Aleksic et al. (2015b).

4.2.4 Radio-optical correlations

Using the long-term OVRO and KVA observations of Mrk 501, Lindfors et al. (2016) reported the optical and radio flares in the same epochs. We constructed the scatter plots with the 15 GHz flux values plotted versus those from the contemporaneous observations performed in the UVOT bands *V*, *B* and *U* during 2009–2016. These plots showed positive correlations with $r = 0.40$ (0.12)–0.48 (0.10). This results is in accord of the suggestion of Lindfors et al. (2016) that at least 10–50 per cent of the optical emission in VHE gamma-ray emitting BLLs originates in the same emission region as the radio, while the other half is due to faster variations not seen in the radio band. Note that the contemporaneous radio and optical observations of Mrk 501 during 2014 March–October were very few, not enough to reveal statistically significant positive radio-optical correlations.

Finally, the UVOT-band fluxes showed a strong correlation to each other with $r = 0.71(0.05)$–$0.88(0.03)$ (see Fig. 7k and Table 9), except for the *V*-band flux that exhibited a moderate correlation with fluxes from the bands $B - UVW2$ with $r = 0.52$ (0.10)–0.68 (0.06). This can be related to the largest host contribution in this band compared to shorter wavelengths, yielding a weaker flux variability in the *V* band and decreasing its correlation with those in the *B–UVW2* bands.

4.3 Spectral variability

4.3.1 Spectral curvature

In 2014 March–October, the parameter *b* mostly showed relatively small values that allows us to draw some conclusion about the acceleration mechanism of X-ray emitting particles. Namely, a curved spectral distribution of the particles with energy develops when the acceleration probability is a decreasing function of the electron energy (so-called energy-dependent acceleration probability process; M04), and a positive correlation between *a* and *b* is expected (found for Mrk 421 from the *BeppoSAX* observations in 1997–1999; M04). However, we have not revealed a significant correlation between these parameters for our target in the period presented here. On

the other hand, a curved spectral distribution can be established via the stochastic acceleration that arises from the magnetic turbulence close to the shock front (T09). Massaro, Paggi & Cavaliere (2011) showed that the electrons in the jets of TeV detected HBLs should undergo a more efficient stochastic acceleration than in those of the TeV-undetected HBLs. The same authors showed that the synchrotron SEDs are relatively broad (i.e. the curvature is smaller with $b \backsimeq 0.3$) when the stochastic acceleration is more efficient while they are narrower ($b \backsimeq 0.7$) in the opposite case. Our study of the curvature parameter from the XRT spectra of Mrk 501 shows its distribution maximum at $b = 0.23$, and majority of the spectra with $b \leq 0.3$, i.e. the source mainly exhibited broad synchrotron SEDs expected when the stochastic mechanism is more efficient. Moreover, we have revealed an anticorrelation between b and $E_{\rm p}$ that is also expected in the case of the effective stochastic acceleration of the electrons responsible for a emission of X-ray photons.

Along with mostly small spectral curvature, the 2014 March–October period is remarkable with a significantly frequent occurrence of the PL spectra in Mrk 501 (24 per cent of all spectra), and M08 reported a more frequent occurrence of these spectra from the *BeppoSAX*, *XMM–Newton* and *Swift*–XRT observations in 1997–2007. The percentage of PL spectra were significantly low in Mrk 421 (13 per cent in 2013 January–April; Kapanadze et al. 2016c), PKS 21554−304 (5 per cent; Kapanadze et al. 2014), 1ES 1959+650 (1.6 per cent in 2005–2104 and only one occasion in 2015 August–2016 January; Kapanadze et al. 2016a,b). This result leads to the suggestion that the jets of these sources should be characterized by physical conditions that are more suitable for a generation of the curved distribution of X-ray emitting particles.

4.3.2 *Position and height of the synchrotron SED peak*

Although a strong spectral variability during X-ray flares is familiar to HBLs, and it has been reported by various authors (see M04; Massaro et al. 2008; T09; Kapanadze et al. 2014, 2016a,b,c), the changes in the position of the synchrotron SED peak in Mrk 501 during the period presented here was one of the most extreme variability ever reported for HBLs: an overall variability by about 20 keV, corresponding to 1.42 order of the frequency, and 95 per cent of the $E_{\rm p}$ values found in hard X-rays. However, our target showed a more extreme spectral variability in 1997 April when the synchrotron SED peak position underwent a shift by at least two orders of the frequency and moved beyond 100 keV (Pian et al. 1998), and the upper limit to $E_{\rm p}$ was not constrained due to the lack of BeppoSAXs of sensitivity in the energy range of $E > 100$ keV (Tavecchio et al. 2001). On the other hand, the smallest value of the parameter $E_{\rm p}$ was 0.34 ± 0.03 keV, derived from the *BeppoSAX* observation performed on 1999 October 6 (M04). Therefore, the overall range of the synchrotron peak location for Mrk 501 is larger than the 2.3 orders of the frequency. This result serves as an evidence for extreme changes in the physical conditions in our target from epoch to epoch, since the SED peak location is related to the jet physical parameters as $E_{\rm p} \propto \gamma_{3{\rm p}}^2 B\delta$ (T09), where $\gamma_{3{\rm p}}$ is the peak of the distribution $n(\gamma)\gamma^3$, B is the magnetic field strength and δ is the Doppler factor. Mrk 421 underwent a very large shift in the SED peak position by about 3.5 orders of the frequency 2013 February–April, but it never exceeded a threshold of 20 keV in contrast to our target (Kapanadze et al. 2016c). A very large value of 21.95 ± 0.60 keV was also found for 1H 1426+428 (Massaro et al. 2008), although the range of the SED peak position is smaller for this source compared to Mrk 421 and Mrk 501 ($\Delta \log \nu_{\rm p} = 1.30$ with $\log \nu_{\rm p} = E_{\rm p}/h$).

According to M08, the detection of the correlation $S_{\rm p} \propto E_{\rm p}^{\alpha}$ may be used to draw a conclusion about the physical factor (variations of the electron average energy/magnetic field/beaming factor/number of emitting particles) that makes the main contribution to the observed spectral variability of the source (depending on the values of the exponent α). The XRT observations of 2014 March–November showed a positive correlation between $S_{\rm p}$ and $E_{\rm p}$ (see Table 7 and Fig. 7l) with $\alpha = 0.50 \pm 0.13$ for Mrk 501. Note that the value of the parameter α is relatively close to the case $S_{\rm p} \propto E_{\rm p}^{0.6}$ when the parameters $D_{\rm p}$ (the momentum-diffusion coefficient) and p (the exponent describing the turbulence spectrum) are variable during the stochastic acceleration process of the particles (see Tramacere, Massaro & Taylor 2011).

4.3.3 *Hard X-ray spectra and spectral evolution with flares*

Our results also show that Mrk 501 exhibited very hard X-ray spectra with the photon index at 1 keV sometimes smaller than $a = 1.50$, and an HR mostly greater than HR = 1 that also rarely happens in BLLs. From the past X-ray observations, Massaro et al. (2008) reported one occasion with $a = 1.41 \pm 0.01$ corresponding to the observation with the highest historical value of the parameter $E_{\rm p}$, and other spectra showed the range of $a = 1.62$–2.15. Note that the largest value of the parameter a was derived from the aforementioned spectrum with the smallest value of $E_{\rm p}$. Among other HBLs, very hard X-ray spectra with $a = 1.34$–1.45 were revealed for Mrk 421 (Ravasio et al. 2004), 1ES 1959+650 (Kapanadze et al. 2016b) and 1ES 2344+514 (Massaro et al. 2008).

Similar to other bright and well-studied HBLs (see e.g. T09; Kapanadze et al. 2014, 2016a,b,c), Mrk 501 mostly exhibited a 'harder-when-brighter' spectral evolution during the flares in the 0.3–10 keV energy range in 2014 March–October. However, the subsamples, corresponding to Periods 2 and 5, do not follow this trend that can be related to the different underlying physical conditions in these periods (see T09 for the corresponding discussion). In the case of the past X-ray studies, a 'harder-when-brighter' behaviour of our target during the *RXTE*-PCA and *XMM–Newton* observations of Mrk 501 in 1997–2000 was reported by Gliozzi et al. (2006), although they also reported an opposite evolution from the flare observed in 1997 July. Moreover, the aforementioned behaviour was evident also during the *Swift*-XRT and *RXTE*-PCA observations performed in 2008 March–May (Aleksic et al. 2015a). Note that the source exhibited a 'harder-when-brighter' spectral evolution also in the HE-VHE part of the spectrum (see Aharonian et al. 2001; Albert et al. 2007; Abdo et al. 2011).

4.3.4 *Hard γ-ray spectra*

Similar to the LAT observations of our target in 2011 (see Shukla et al. 2015), Mrk 501 often showed very hard γ-ray spectra with the 0.3–300 GeV photon index $\Gamma < 1.70$. According to Shukla et al. (2015), a hard γ-ray spectrum could be obtained much more easily within the hadronic scenarios, whereas achieving a hard spectrum from leptonic models is more demanding. For example, the proton blazar model introduced by Mannheim (1993) predicts the generation of the X-ray spectra with the photon index of 1.5–1.7 that was often shown by our target during 2014 March–October. However, this model is challenged by correlated TeV–X-ray variability, often observed in this epoch. Furthermore, the source showed an extreme

TeV IDV with a flux doubling time of a few minutes on June 23–24, and it is difficult to produce a subhour flux variability with hadronic models (see e.g. Aleksic et al. 2015c). Very hard spectra, in combination with the subhour flux variability, was successfully explained via the two-zone SSC scenario developed by Shukla et al. (2016) for Mrk 501 that demonstrated that a fast 5 min to 1 h variability with a hard spectrum should be related to the jet base where the electrons can be accelerated to VHE via the second-order (stochastic) *Fermi* mechanism. In that case, low values of the curvature parameter b in the X-ray band is predicted (see Section 4.4) that is in agreement with our spectral results obtained for the fast X-ray IDVs (see Table 4).

4.4 Spectral hysteresis

The analysis of hysteresis patterns in the HR–flux plane is useful for drawing conclusions about the interplay between electron acceleration ($\tau_{\rm acc}$), synchrotron cooling ($\tau_{\rm syn}$) and flux variability ($\tau_{\rm var}$) time-scales. In this plane, one may observe following spectral hysteresis loops (Cui 2004): (a) a CW loop, if $\tau_{\rm syn} \gg \tau_{\rm var} \gg \tau_{\rm acc}$, or $\tau_{\rm syn} \gg \tau_{\rm acc} \gg \tau_{\rm var}$. In this case, the spectrum becomes softer in the flux declining phase and harder along with the brightening, indicating that the variations of the hard X-rays always lead those in the soft X-rays both during the increase and decrease of the brightness of the source (Takahashi et al. 1996); (b) a CCW loop, when $\tau_{\rm syn} \approx \tau_{\rm acc} \approx \tau_{\rm var}$. The information about the occurrence of a flare propagates from lower to higher energies, as particles are gradually accelerated, while a brightness decline can be dominated by the particle escape effects, and we should observe a hard lag (Ravasio et al. 2004).

Our study of the hysteresis patterns in Mrk 501 shows that the extreme spectral variability observed in 2014 March–October was related to the acceleration and cooling time-scales of emitting particles in a complex manner. Fig. 10 exhibits that some flares had a cooling time acting faster at higher energies, and this situation is consistent with the dominance of synchrotron cooling, since its time-scale is shorter at higher energies (Falcone et al. 2004), and the source followed a CW loop in the HR–flux plane. A CCW-type evolution should be due to the flaring component starting in the hard X-ray band, triggered by a rapid injection of very energetic particles rather than by a gradual acceleration, when a CW-type evolution is expected (see T09), and our target showed CCW-type loops several times during 2014 March–October. During the past X-ray studies of Mrk 501, no clearly expressed CW or CCW loops were found by Xue & Cui (2005) from the *RXTE*-ASM observations performed in 1997. From the *RXTE*-PCA and *XMM–Newton* observations of Mrk 501 in 1997–2000, Gliozzi et al. (2006) reported the presence of CW loops during the 1998 June and 1999 May flares, and no signs of hysteresis loops were found in other cases.

5 CONCLUSIONS

In this paper, we report about the most powerful and prolonged X-ray flaring activity in Mrk 501 observed with *Swift*-XRT during the 11.5-yr period since the start of its monitoring. During 2014 March–October, a new largest historical 0.3–10 keV count rate was recorded twice that made this object the second BLL exceeding the level of 20 cts s^{-1}. This epoch was characterized by short-term X-ray flares by a factor of 1.9–4.7 on time-scales of a few weeks and by 35 instances of intraday variability with the fractional variability amplitudes of 2.8–29.7 per cent, which sometimes occurred within the 1-ks interval. For the whole period, the fractional variability amplitude shows a double-humped shape with the highest variability in the X-ray and VHE bands, interpreted as resulting from a correlation between the synchrotron and IC peaks of the broad-band SED. The XRT and FACT observations mainly showed a correlated variability, also one occasion of the uncorrelated TeV-X-ray variability is also found. The LAT-band and optical-UV fluxes mostly showed an uncorrelated variability with the X-ray one, while there was a positive correlation between the 0.3–300 GeV and UVOT-band fluxes (expected in the case of the KN suppression in the IC process, yielding an effective upscatter of optical-UV photons to the GeV energies by the electrons, radiating in X-rays).

Along with a strong flux variability, the source also showed an extreme spectral behaviour. The majority of the 0.3–10 keV spectra were curved, and the position of the SED peak showed an overall variability by about 20 keV, and 95 per cent of the $E_{\rm p}$ values were found in the hard X-ray part of the spectrum. Both LP and PL spectra often were very hard with the photon index smaller than $a = 1.70$. The HR was mostly greater than HR $= 1$ that is also uncommon for HBLs. Both parameters showed a strong variability on various time-scales, and the source mainly exhibited a 'harder-when-brighter' spectral evolution, although two short-term X-ray flares did not show any clearly expressed trend. Mrk 501 mostly showed a relatively small X-ray spectral curvature and an anticorrelation with the position of the synchrotron SED, expected in case of the effective stochastic acceleration of the electrons from the magnetic turbulence close to the shock front.

Our study of the hysteresis patterns in Mrk 501 revealed that short-term flares and extreme spectral variability in 2014 March–October were related to a complex and variable interplay between the acceleration and cooling time-scales of emitting particles. Some flares showed the patterns of gradual acceleration and the dominance of synchrotron cooling with possible soft lags, while a rapid injection of very energetic particles and possible hard lags can be suggested for other flares.

We conclude that Mrk 501 is one of the most extreme HBLs with a very strong and complex spectral variability, unpredictable flux variability and exclusively strong X-ray flares in some epochs. These properties underline the importance of further intensive MWL campaigns of our target that will be very useful for gaining a deeper understanding of the AGN phenomenon and blazar physics.

ACKNOWLEDGEMENTS

BK, SK and LT acknowledge Shota Rustaveli National Science Foundation and Ilia State University for the fundamental research grant FR/377/6-290/14. KM and DD acknowledge the funding by the German BMBF (Verbundforschung Astro- und Astroteilchenphysik) and HAP (Helmholtz Alliance for Astro-particle Physics). PR acknowledges the contract ASI-INAF I/004/11/0. We acknowledge the helpful service of HEASARC, and the use of public data from the *Swift* and *Fermi* archives. This research has made use of the XRTDAS software, developed under the responsibility of the ASDC, Italy, and the data from the OVRO 40-m monitoring programme that is supported in part by NASA grants NNX08AW31G and NNX11A043G, and NSF grants AST-0808050 and AST-1109911. In our study, the data from the Steward Observatory spectropolarimetric monitoring project supported by *Fermi* Guest Investigator grants NNX08AW56G, NNX09AU10G, NNX12AO93G and NNX15AU81G were used. We thank the FACT Collaboration for making their analysis results publicly available, and appreciate their long-term monitoring initiative that provides precious input for

MWL studies. We thank the anonymous referee for his/her very useful comments and suggestions that helped to improve the quality of the paper.

REFERENCES

Abdo A. A. et al., 2011, ApJ, 727, 129
Acero F. et al., 2015, ApJS, 218, 23
Aharonian F. A. et al., 1999, A&A, 349, 11
Aharonian F. A. et al., 2001, ApJ, 546, 898
Albert J. et al., 2007, ApJ, 669, 862
Aleksic J. et al., 2015a, A&A, 573, 50
Aleksic J. et al., 2015b, A&A, 576, 176
Aleksic J. et al., 2015c, A&A, 578, 22
Anderhub H. et al., 2009, ApJ, 725, 1624
Andruchow I., Romero G. E., Cellone S. A., 2005, A&A, 442, 57
Atwood W. B. et al., 2009, ApJ, 697, 1071
Baloković M. et al., 2016, ApJ, 819, 156
Barthelmy S. D. et al., 2005, Space Sci. Rev., 120, 143
Bartoli B. et al., 2012, ApJ, 758, 2
Bartoli B. et al., 2016, ApJS, 222, 6
Blandford R. D., Rees M. J., 1978, in Wolfe A. M., ed., Pittsburgh Conf. on BL Lac Objects. Univ. Pittsburgh, Pittsburgh, PA, p. 328
Breeveld A. A. et al., 2011, in McEnery J. E., Rascusin J. L., Gehrels N., eds, AIP Conf. Ser. Vol. 1358, Gamma Ray Bursts 2010. Am. Inst. Phys., New York, p. 373
Burrows D. N. et al., 2005, Space Sci. Rev., 120, 165
Catanese M. et al., 1997, ApJ, 487, L143
Catanese M., Sambruna R., 2000, ApJ, 534, L39
Chakraborty N. et al., 2015, preprint (arXiv:1509.04893)
Chiappetti L. et al., 1999, ApJ, 521, 552
Cui W., 2004, ApJ, 605, 662
Dermer C. D., Schlickeiser R., Mastichiadis A., 1992, A&A, 256, L27
Dorner D. et al., 2015, preprint (arXiv:1502.02582)
Falcone A. D., Cui W., Finley J. P., 2004, ApJ, 601, 165
Falomo R., Pian E., Treves A., 2014, A&AR, 22, 37
Fink H. H., Thomas H.-C., Hasinger G., Predehl P., Schaeidt S., Makino F., Warwick R. S., 1991, A&A, 246, L6
Fitzpartick E. L., Messa D., 2007, ApJ, 663, 320
Furniss A. et al., 2015, ApJ, 812, 65
Gehrels N. et al., 2004, ApJ, 611, 1005
Gliozzi M., Sambruna R. M., Jung I., Krawczynski H., Horan D., Tavecchio F., 2006, ApJ, 646, 61
Güver T., Özel F., MNRAS, 400, 2050
Kalberla P. M. W., Burton W. B., Hartmann D., Arnal E. M., Bajaja E., Morras R., Pöppel W. G. L., 2005, A&A, 440, 775
Kapanadze B., Romano P., Vercellone S., Kapanadze S., 2014, MNRAS, 444, 1077
Kapanadze B., Romano P., Vercellone S., Kapanadze S., Mdzinarishvili T., Kharshiladze G., 2016a, MNRAS, 457, 704
Kapanadze B., Dorner D., Vercellone S., Romano P., Kapanadze S., Mdzinarishvili T., 2016b, MNRAS, 461, L26
Kapanadze B. et al., 2016c, ApJ, 831, 102
Krim H. et al., 2013, ApJ, 209, 14
Lindfors E. J. et al., 2016, A&A, 593, 98
Mangalam A. V., Wiita P. J., 1993, ApJ, 406, 420
Mannheim K., 1992, A&A, 269, 67
Mannheim K., Biermann P. L., 1992, A&A, 253, L21
Marscher A. P., Gear W. K., 1985, ApJ, 298, 114
Massaro E., Perri M., Giommi P., Nesci R., 2004, A&A, 413, 489 (M04)
Massaro F., Tramacere A.; Cavaliere A., Perri M., Giommi P., 2008, A&A, 478, 395
Massaro F., Paggi A., Cavaliere A., 2011, ApJ, 742, L32
Max-Moerbeck W., Richards J. L., Hovatta T., Pavlidou V., Pearson T. J., Readhead A. C. S., 2014, MNRAS, 445, 437
Nilsson K., Pasanen M., Takalo L. O., Lindfors E., Berdyugin A., Ciprini S., Pforr J., 2007, A&A, 475, 199
Padovani P., Giommi P., 1995, ApJ, 444, 567
Perlman E. S. et al., 2005, ApJ, 625, 727
Pian E. et al., 1998, ApJ, 492, L17
Poole T. S. et al., 2008, MNRAS, 383, 627
Quinn J. et al., 1996, ApJ, 456, L83
Ravasio M., Tagliaferri G., Ghisellini G., Tavecchio F., 2004, A&A, 424, 841
Richards J. L. et al., 2011, ApJS, 194, 209
Roming P. W. A. et al., 2005, Space Sci. Rev., 120, 95
Sambruna R. et al., 2000, ApJ, 538, 127
Shukla A. et al., 2015, ApJ, 798, 2
Shukla A., Mannheim K., Chitnis V. R., Roy J., Acharya B. S., Dorner D., Hughes G., Biland A., 2016, ApJ, 832, 177
Smith P. S. et al., 2009, Fermi Symposium, eConf Proceedings C091122
Sokolov A., Marscher A. P., McHardy I. M., 2004, ApJ, 613, 725
Takahashi T. et al., 1996, ApJ, 470, L89
Tavecchio F. et al., 2001, ApJ, 554, 725
Tramacere A., Giommi P., Perri M., Verrecchia F., Tosti G., 2009, A&A, 501, 879 (T09)
Tramacere A., Massaro E., Taylor A. M., 2011, ApJ, 739, 66
Ulrich M. H., Kinman T. D., Lynds C. R., Rieke G. H., Ekers R. D., 1975, ApJ, 198, 261
Vaughan S., Edelson R., Warwick R. S., Uttley P., 2003, MNRAS, 345, 1271
Villata M., Raiteri C. M., Lanteri L., Sobrito G., Cavallone M., 1998, A&AS, 130, 305
Wagner S., Witzel R., 1995, ARA&A, 33, 163
Xue Y., Cui W., 2005 ApJ, 622, 160

SUPPORTING INFORMATION

Supplementary data are available at *MNRAS* online.

Table 1. Extract from the summary of the XRT observations of Mrk 501 in 2014 March–October.
Table 2. Extract from the results of the UVOT observations.
Table 4. Extract from the summary of IDVs at the 99.9 and 99.5 per cent confidence levels from the XRT observations of Mrk 501.
Table 5. Extract from the summary of the XRT spectral analysis with the LP.
Table 8. Extract from the summary of the XRT spectral analysis with a simple PL model.
Figure 9. Photon index, HR, the position of the synchrotron SED plotted versus time in different periods discussed in Section 3.1.3.
Figure 10. Spectral hysteresis in different epochs with the soft 0.3–2 keV (black points) and hard 2–10 keV (grey points) fluxes plotted versus time (extract).

Please note: Oxford University Press is not responsible for the content or functionality of any supporting materials supplied by the authors. Any queries (other than missing material) should be directed to the corresponding author for the paper.

This paper has been typeset from a TEX/LATEX file prepared by the author.